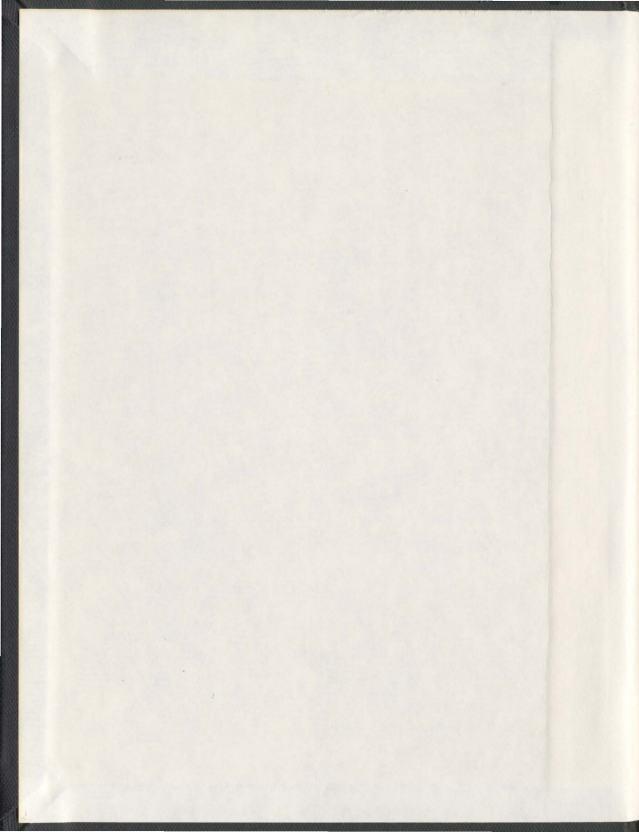
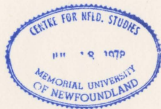


ELECTROCHEMICALLY ASSISTED ASSEMBLY OF
COLLAGEN MEMBRANES AND COLLAGEN-CALCIUM
PHOSPHATE COMPOSITE MATERIALS

RAMESH KUMAR MANI



001311



**Electrochemically assisted assembly of collagen
membranes and collagen-calcium phosphate
composite materials**

by

©Ramesh Kumar Mani

A Thesis submitted to the School of Graduate Studies in partial fulfillment of the
requirements for the degree of

Doctor of Philosophy

Department of Chemistry
Memorial University of Newfoundland

December 2011

St. John's

Newfoundland

*This thesis is dedicated to my beloved father, Mr. P. Mani
and brother, M. Saravana Kumar.*

Abstract

I have designed bioactive collagen-based materials using electrochemical synthesis methods. Preparation of these collagenous materials involves assembly of fibrils from collagen monomers; inorganic-protein composites can be formed by subsequent electrochemically induced precipitation of calcium phosphate minerals. These collagen-calcium phosphate composites are stiffer than the original collagen membranes. The electrochemically assisted mineral precipitation can yield several different calcium phosphate phases (including hydroxyapatite, brushite, or amorphous calcium phosphate) depending on electrolyte composition. Change in the electrolyte composition (by adding different ions), electrolyte pH or duration of the applied field produces membranes with a range of Young's moduli. Single particle tracking reveals that changing the electrolyte composition changes the internal pore structure of the formed collagen membrane. Biocompatibility studies show that cells grow very well on the electrochemically aggregated collagen membranes when they are used as a supportive matrix. Since a major portion of a cornea is made up of collagen, our collagen membranes may be useful as a matrix for artificial cornea applications.

Acknowledgements

First and foremost, I would like to express my sincere gratitude to my supervisors Prof. Erika F. Merschrod S and Prof. Kristin M. Poduska for their support, guidance and invaluable assistance throughout my thesis work, and without their help it would not have been possible for me to complete this dissertation. They both were always accessible, ready to help students with their research at anytime, which made my research life at this university very smooth.

Besides my advisors, Prof. Christopher Kozak and Prof. Yuming Zhao deserve a special thanks for being my supervisory committee members, providing their suggestions during the program and spending their time for the evaluation of this report.

It is an honor for me to thank Prof. Robert Gendron and Prof. Hélène Paradis, MUN Medicine for having collaboration and showing much interest in this work.

I am grateful to all my lab mates, especially Holly Baker, Asim Rasheed, Chuan Xu, Behrang moazez, Shaheen Fathima, Alina Stetco, Jiaqi Cheng and Tiju Thomas for sharing their literature and knowledge, and for maintaining the lab environment very peaceful to work. I also thank my other friends who assisted me in any respect during the program.

I owe my deepest gratitude to my mom, Mrs. Meenambigai, and sister, Mrs. Jamunarani for their endless love, support and understanding throughout my studies. Also, I could not have done this work without the inspirations and support from my wife, Vidya, whose love and patience has been my nourishment through the most difficult times.

I take this opportunity to thank Ms. Julie Collins, Mr. Brent Myron and Mr. Nick Ryan for the training and assistance with Differential Scanning Calorimeter and IR spectroscopy.

Furthermore, I would like to thank Department of Chemistry, Memorial University

of Newfoundland, Canada Foundation for Innovation (CFI) and the Natural Sciences and Engineering Research Council of Canada (NSERC) for financial support.

Table of Contents

	i
Abstract	iii
Acknowledgments	iv
Table of Contents	x
List of Tables	xiii
List of Figures	xxiv
1 Introduction to collagen and collagen-calcium phosphate materials	1
1.1 Collagen	2
1.1.1 Structure of collagen	2
1.1.2 Hierarchical assembly of collagen	3
1.1.3 <i>In vitro</i> collagen assembly methods	5
1.1.3.1 Magnetic alignment	5
1.1.3.2 Electro-spinning process	6
1.1.3.3 Liquid crystalline ordering	6
1.1.3.4 Microfluidic alignment	6
1.1.3.5 Electrochemical aggregation	7

1.1.4	Mechanism of electrochemical collagen membrane formation . . .	8
1.1.5	Atomic force microscopy for imaging collagen	10
1.2	Bone implants based on collagen-calcium phosphate composites . . .	12
1.2.1	Target properties for effective bone implants and coatings . . .	13
1.2.2	Overview of synthesis methods for bone implants and coatings	14
1.2.2.1	Thermal synthesis	14
1.2.2.2	Solution-phase synthesis	15
1.2.2.3	Electrochemically assisted synthesis	15
1.2.3	Electrochemically prepared biominerals	16
1.3	Overview of the thesis	17
	References	18

2	Correlating mechanical properties with aggregation processes in electrochemically fabricated collagen membranes	26
2.1	Introduction	26
2.2	Experimental method	29
2.2.1	Sample preparation	29
2.2.2	Optical characterization	30
2.2.3	Atomic Force Microscopy	30
2.2.4	Modeling stiffness	32
2.2.4.1	Hertzian model	32
2.2.4.2	Oliver-Pharr model	33
2.3	Model force curve calculation	34
2.4	Results	41
2.4.1	Membrane formation	41
2.4.2	Correlating mechanical stiffness with fibril content	43
2.4.3	Ion-dependent softening and stiffening	48

2.5	Discussion and conclusions	54
	References	56
3	Collagen-membrane-induced calcium phosphate electrocrystallization	59
3.1	Introduction	59
3.2	Experimental procedure	60
3.3	Results and discussion	62
3.3.1	Electrolyte composition and concentration effects	62
3.4	Phase selectivity	63
3.4.1	Collagen membrane's role in mineral growth	64
3.4.2	Collagen membrane's role in mineral nucleation	68
3.5	Conclusions	69
	References	69
4	Towards an artificial cornea: Electrochemical engineering of a collagen scaffold	71
4.1	Introduction	72
4.2	Experimental	73
4.2.1	Preparation of matrix scaffolds	73
4.2.2	Characterization techniques	74
4.2.2.1	Differential scanning calorimetry (DSC)	74
4.2.2.2	UV-vis spectroscopy	74
4.2.2.3	Scanning electron microscopy (SEM)	74
4.2.2.4	Cell culture studies	76
4.3	Results and discussion	76
4.3.1	Thermal stability of collagen membrane	76
4.3.2	Optical transparency of collagen membrane	78

4.3.3	Morphology of collagen membrane	78
4.3.4	Cell viability	78
4.3.5	Controlled cell proliferation	81
4.4	Conclusions	81
	References	83
5	Analyzing the internal pore structure of collagen membranes using single particle tracking (SPT)	85
5.1	Introduction	85
5.1.1	Trajectories for possible internal structures of membranes	90
5.2	Methods and experimental procedure	91
5.2.1	Sample preparation	91
5.2.1.1	Preparation of fluorescent bead solutions	91
5.2.1.2	Preparation of collagen membrane incorporating fluo- rescent beads	92
5.2.2	Instrumentation	93
5.2.3	Data analysis	94
5.3	Results and discussion	95
5.3.1	Optimizing particle and trajectory identification	95
5.3.2	Validating the setup: particle tracking in water	99
5.4	Pore-size analysis for collagen membranes	100
5.4.1	Pore shapes/interconnectedness	105
5.4.2	Diffusion constants and membrane pore-liquid viscosities	108
5.5	Conclusions	111
	References	111
6	Conclusions	114

6.1 Summary	114
6.2 Future directions	117
References	118
A Studying the effects of different cations on structure and mechanical properties	120
References	125
B Collagen-hydroxyapatite vs. collagen-brushite composites	126
References	130

List of Tables

1.1	Selected calcium phosphate phases	13
2.1	Representative Young's moduli (E) extracted from the slopes of force-displacement data using the Hertzian contact model for a collagen membrane prepared from pH 7 electrolyte using 30 minutes of applied voltage.	38
2.2	Representative Young's moduli and related parameters extracted from force curve data using the Oliver-Pharr model for collagen membranes prepared from pH 7 electrolyte using 30 minutes of applied voltage. For all curves, we use $\varepsilon = 0.75$ for our paraboloid indenter, in accordance with References [20, 21], and a cantilever spring constant $K_C = 16.87$ N/m.	40
2.3	T-test comparisons of the elastic moduli (Oliver-Pharr) of collagen membranes prepared using different pH electrolytes.	48
2.4	T-test comparisons of the elastic moduli (Hertzian) of collagen membranes prepared with the addition of various salts.	50

3.1	Comparison of mineral products resulting from an electrochemically (EC) produced collagen membrane composite, electrochemically assisted precipitation or solution precipitation using different starting electrolytes. Control experiments performed with a cellulose membrane did not yield a measurable amount of mineral on the membrane. . . .	63
5.1	Excitation and emission wavelengths and the supplier of various size fluorescent beads that we use for our experiments. All the beads are made of polystyrene and are stabilized by sulfate groups. ^{16, 17}	91
5.2	Concentration of prepared bead solution, and the concentration of beads in the final collagen monomer electrolyte for various sized beads.	92
5.3	Pore size and pore area calculation for selected trajectories in the collagen membrane prepared with 0.92 μm fluorescent beads. The minimum and maximum x and y values in the trajectory plot (Figure 5.9a) are used to calculate the approximate pore diameter in the x and y directions and approximate pore area. The bead diameter (0.92 μm) is added to the trajectory-obtained value to get the original pore size. Multiple trajectories give information about different pores in the membrane.	103
5.4	T-test comparisons for the pore areas of various collagen membranes.	104

5.5	Summary of the pore size and pore area calculations done using different size beads for various collagen membranes prepared with and without addition of KCl or CaCl ₂ salts. The table shows that the pore size and area are similar for normal and softer membranes, and the pores are larger for the stiffer membrane. Small beads give larger pore values because they can move efficiently inside the pores and can reach all the corners of pores more easily than larger beads. SD denotes standard deviation.	107
5.6	Diffusion constant and membrane pore-liquid viscosity calculations performed using different size beads for the collagen membranes prepared with and without addition of KCl or CaCl ₂ salts. The smaller beads diffuse well in the pores of the collagen membrane, thus giving higher <i>D</i> values. The diffusion constant is calculated from the slope of MSD <i>vs.</i> time plots (Figure 5.12), and the viscosity is calculated using Equation 5.1.	108
5.7	T-test comparisons for the liquid viscosities (η) in the pores of normal, softer and stiffer collagen membranes.	110

List of Figures

- 1.1 Zwitterionic structures of (a) glycine, (b) *L*-proline and (c) trans-4-hydroxy-*L*-proline. 3
- 1.2 Schematic diagram for the hierarchical assembly of collagen fiber from collagen monomer. Image is modified from Reference [31]. 4
- 1.3 Schematic diagram of a two-electrode electrochemical cell. A collagen monomer solution is used as the electrolyte, and two polished stainless steel plates are used as electrodes. Once potential is applied to the collagen electrolyte, a highly aligned, mechanically robust collagen membrane can form parallel to the anode and cathode. 7
- 1.4 Schematic of the electrochemical membrane formation process. (a) Collagen molecules in the acidic side get a negative charge and the molecules in the basic side gain a positive charge due to the *pH* gradient. (b) A collagen membrane forms by migration of collagen monomers driven by an applied field between the two electrodes. 9
- 2.1 A schematic diagram of possible membrane formation pathways. Monomers can either aggregate (A) non-specifically or (B) hierarchically to form protofibrils (thickness of ~ 5 nm) and then fibrils (thickness of ~ 100 nm). Non-specific aggregates do not lead to fibril formation. 28

2.2	Schematic diagram of the nanoindentation process. a is contact area radius, h_c is true contact depth and h is measured depth. Image is modified from References [19, 20].	35
2.3	(a) A representative force-displacement curve obtained on a collagen membrane prepared from pH 7 electrolyte using 30 minutes of applied voltage. The dashed line is the extension curve, and the solid line is the retraction curve. The inset highlights the hysteresis between extension and retraction at the first and last points of probe-membrane contact. (b) Fitting the retraction curve to a power law expression yields a power coefficient $m = 1.6 \pm 0.1$, which is appropriate for a paraboloid indenter.	37
2.4	More acidic pH values (a) and lower ionic strengths (b) increase the amount of time required for membrane formation. The lines connecting the data points serve as guides to the eye and the uncertainty estimates associated with each data point in (b) are contained within the size of the markers.	41
2.5	UV-Vis absorption spectra of post-deposition electrolytes show that longer exposure to the applied potential leads to a decrease in the collagen-related absorbance peak near 200 nm (inset), corresponding to more collagen incorporation into the membrane. The marker spacings on the ordinate axes are consistent for the main graph and the inset.	42
2.6	Young's modulus values for electrosynthesized collagen membranes change as two parameters were varied independently: (a) duration of applied voltage (at pH 7) and (b) initial electrolyte pH value (for 30 minute voltage duration). Error bars correspond to a set of measurements made with the same tip on the same sample. Trends are qualitatively similar using either Hertzian or Oliver-Pharr models for tip-sample contacts.	44

2.7	Raman spectra from collagen samples prepared with (a) different durations of applied voltage (all at pH 7) and (b) electrolytes with different initial pH values (all with 30 minutes of applied voltage). Spectra are offset along the intensity axis for clarity. Estimates of fibril to monomer ratio based on peak height comparisons from these spectra show (c) more distinctive fibril signatures for longer duration of applied voltage, and (d) a slight decrease of fibril content when the electrolyte pH is near the isoelectric point of collagen.	46
2.8	Young's moduli values can change dramatically with the addition of different concentrations of (a) CaCl ₂ or (b) KCl, with smaller changes for the addition of (c) NaCl to the electrolyte. Stiffness trends follow changes in the relative amount of fibrillar collagen (d, as determined from Raman scattering peak intensities), with stiffer membranes displaying higher fibril content.	49
2.9	Representative AFM images of dried electrolyte aliquots obtained immediately before visible membrane formation (5 minutes of applied electric field) in electrolytes containing (a) 10 mM Ca ²⁺ , (b) no Ca ²⁺ or K ⁺ , and (c) 10 mM K ⁺ . Fibrillar topographic features are least prevalent in the 10 mM Ca ²⁺ aliquot, even though the membranes produced from that electrolyte show the highest relative fibril content in Raman data.	52

2.10	<p>Representative AFM images show that fibrils grow when in the presence of an applied electric field, both in the electrolyte (a,b) and in the membrane itself (c,d,e). All images shown here are from experiments with electrolytes containing 10 mM Ca^{2+}. Dried electrolyte aliquots show more fibrils in both the (a) alkaline and (b) acidic electrolytes. Images of the outermost layer of the membrane formed in 15 minutes (c) or 30 minutes (d) show less fibril content. The ethanol rinsed membrane (e) shows considerably more fibrillar topographies.</p>	53
3.1	<p>A schematic illustration of the two-step process for preparing the membrane-based electrosynthesized collagen-mineral composite. An applied voltage is required both to form the collagen membrane (Step 1) and to stimulate crystallization of the calcium phosphate on the membrane (Step 2). The acidic and basic regions are produced by water electrolysis and are maintained after the membrane forms.</p>	61
3.2	<p>(a) Representative IR spectra for collagen-calcium phosphate composites prepared with collagen monomers plus 0.1 M CaCl_2 and either 0.1 M (i) K_2HPO_4 or (ii) $\text{NH}_4\text{H}_2\text{PO}_4$ show that precursor salts affect phase selectivity. The dominant peaks in spectrum (i) are from carbonated hydroxyapatite (CHAp) while those in (ii) indicate brushite. (b) Representative IR Spectra for specimens prepared using CaCl_2 and K_2HPO_4, either without (i) or with (ii) collagen, highlight the importance of the presence of collagen for phase selectivity. CHAp forms in the presence of collagen; otherwise, amorphous calcium phosphate (ACP) dominates. In both panels, spectra are offset along the absorbance axis for clarity.</p>	65

3.3	Representative SEM micrographs, at low (a, b) and high (c, d) magnifications, of a carbonated hydroxyapatite-collagen composite (here, from $\text{Ca}(\text{NO}_3)_2$ and $\text{NH}_4\text{H}_2\text{PO}_4$ precursors). The secondary electron images (a, c) show that composite topography is dominated by micron and sub-micron crystallites that appear to be embedded in the protein scaffold. The companion backscattered electron images of the identical areas (b, d) confirm that the mineral, indicated by bright regions, is spread rather uniformly throughout the scaffold.	67
3.4	Comparison of elastic modulus values for composite mineralized collagen membranes (solid line) and unmineralized collagen membranes (dashed line). Preparing an unmineralized membrane in the presence of higher amounts of Ca^{2+} will lead to a slightly stiffer scaffold, but composite membranes are consistently more stiff. The lines connecting data points serve merely to guide the eye.	68
4.1	Schematic diagram for cell culture procedure. First, the collagen matrix scaffolds are prepared by an isoelectric focusing method. After synthesis, the membranes are removed using tweezers and stored in a cell culture petri dish at 4 °C. The membranes are sterilized by UV radiation to remove any biological contamination. The cell culture medium is prepared by using 10% fetal bovine serum (FBS), and the cells are grown in the culture medium with and without the collagen matrix. Cell culture is performed by placing the cell culture dishes in a tissue cell culture incubator for 48 hours in a humid, 5% CO_2 atmosphere at 37.0 °C.	75

4.2	DSC thermogram of a hydrated electrochemically prepared collagen membrane shows a broad and complex protein denaturation peak at 48.6 °C.	77
4.3	UV-vis transmittance spectrum of a hydrated collagen membrane shows the wet membrane is highly transparent and transmits more than 90% of light through it in the visible region (380–750 nm).	79
4.4	Representative scanning electron microscopy images, at two different magnifications (a) 1000x and (b) 10000x, of dried electrochemically prepared collagen matrix scaffolds highlight their sheet-like character. The scale bar in (a) is 200 μm long, and that in (b) is 20 μm long.	79
4.5	(a,b) Phase contrast optical microscopy images of MK/T-1 cells grown in 10% FBS cell culture media with and without presence of the collagen scaffold matrix show that the cells grow very well over the collagen matrix (a), similar to the cells cultured in cell culture plastic (b). Panels (a) and (b) have the same scale. (c,d) Phase contrast optical microscopy images of H&E stained sections of cultured cells; (c) in collagen matrix; (d) on plastic. The images show that the cells prefer to adhere at the edges of the collagen scaffold rather than growing over them. Panels (c) and (d) have the same scale.	80
4.6	(a,b) Phase contrast optical microscopy images of MK/T-1 cells grown in presence of Bromodeoxyuridine(BrdU); (a) in plastic and (b) in collagen matrix. The BrdU staining is less pronounced in the matrix grown cells compared to the cells grown in plastic, which confirms that the collagen scaffold does not allow the cells to proliferate. Cells are indicated with arrows and 'm' denotes the matrix. Panels (a) and (b) have the same scale.	82

5.1	The plot of mean-square displacement, $\langle R^2 \rangle$ as a function of time has a slope which, at early times at least, equals $4D$ (as defined by Equation 5.5). The functional form at longer time varies for different motion modes. The diffusion constant D is higher for flow assisted diffusion and lower or almost zero for confined motion. Image is modified from Reference [3].	87
5.2	After taking hundreds of fluorescence images, the trajectories of the fluorescent bead movement in an environment can be established. Depending on parameters like pore size or matrix viscosity, the bead can move in different ways. Four different types of motion are shown here: (a) directed motion, (b) random walk, (c) confined motion and (d) intermittent or hopping random motion. Image is modified from Reference [15].	89
5.3	Schematic diagram of working principle of particle tracking experiment. A lens is used to convert the cylindrical light beam into a light sheet. When the sample is placed under this optical light sheet, the fluorescent particles in the sample are excited, and subsequently they emit fluorescence during relaxation. A Charge Coupled Device (CCD) camera is used to capture the fluorescence from the particles, and capturing a number of images over a given time provides an idea about the motion of the particles. By finding the positions of a particular bead in subsequent frames, the particle trajectory can be obtained. Image is modified from Reference [18].	93

5.4	Full size (a) and cropped (b) fluorescence microscope images of a fluorescent bead solution. The bright white dots are from the fluorescent beads, and the dark gray area is the solution background. The cropped image shows fewer bright spots, and the spots are enlarged. The diameter of the fluorescent beads is $0.92 \mu\text{m}$, and the concentration of the fluorescent beads in the final electrolyte solution is 1820 ± 130 particles/ μL . (c) All the bright spots in (b) are identified correctly and circled.	96
5.5	Trajectories of fluorescent beads in solution. Different colored trajectories show the motion of different fluorescent beads in both x and y directions.	98
5.6	(a) Trajectory of a fluorescent bead in solution shows that the motion of the bead is a random walk, and the bead can move in any direction between the frames. (b) Mean square displacement (MSD) vs. time plot for a fluorescent bead in solution. This curve is fitted against Equation 5.6 and the obtained D and v are $0.55 \mu\text{m}^2/\text{s}$ and $0.26 \mu\text{m}/\text{s}$ respectively.	99
5.7	Fluorescence image of a collagen membrane in which $0.92 \mu\text{m}$ fluorescent beads are incorporated. The bright spots are from the fluorescent beads, and the black or gray area is the collagen membrane. The image shows that the beads are dispersed well, and individual beads are clearly visible everywhere in the membrane except in a few areas where several beads are aggregated in clusters (see the top-right corner of the image).	101
5.8	(a) Cropped image of Figure 5.7. (b) Trajectories of $0.92 \mu\text{m}$ beads in the collagen membrane.	101

5.9	Particle trajectories of (a) $0.92 \mu\text{m}$ and (b) $0.54 \mu\text{m}$ beads in a collagen membrane show that the particles move randomly in the pores of membrane, and that the size of the pore is $2\text{--}3 \mu\text{m}$	102
5.10	Particle trajectories of $0.92 \mu\text{m}$ beads in a collagen membrane that is prepared with the addition of 0.05 M KCl . Trajectory (a) shows that the beads move randomly inside the pores of collagen membrane. Moreover, the pore sizes ($2\text{--}5 \mu\text{m}$) are similar to the pore sizes of the regularly prepared collagen membrane. Trajectory (b) shows that some membrane pores are interconnected such that a bead can escape from one pore and get into another pore.	105
5.11	Particle trajectory of $0.92 \mu\text{m}$ bead in a collagen membrane prepared with the addition of 0.05 M CaCl_2 shows that the particle moves randomly in membrane pores, and the size of the pore is $\sim 4.5 \mu\text{m}$ including the diameter of the bead.	106
5.12	MSD <i>vs</i> time plots of (a) $0.92 \mu\text{m}$ and (b) $0.54 \mu\text{m}$ beads in the pores of a collagen membrane. MSD <i>vs.</i> time plot for the motion of a $0.92 \mu\text{m}$ bead in a collagen membrane prepared with the addition of (c) 0.05 M KCl or (d) 0.05 M CaCl_2	109
A.1	Atomic Force Microscopy (AFM) images of collagen membranes prepared with and without the addition of excess ions. (a) AFM image of a collagen membrane prepared without any added salt shows no fibrils. AFM images of the collagen membranes prepared with (b) Ca^{2+} or (c) Na^+ show fibrils. (d) K^+ ions in the electrolyte do not lead to fibril formation in the membrane.	121

A.2	AFM images of collagen membranes prepared with different applied potential durations. (a) Collagen membrane prepared with an applied potential duration of 15 minutes does not have any fibrils. (b) AFM image of a collagen membrane prepared with an applied potential duration of 60 minutes shows many fibrils.	122
A.3	Elastic moduli values can change dramatically with the addition of different concentrations of ions such as Mg^{2+} or Ba^{2+} during membrane formation. The presence of Ba^{2+} in the electrolyte increases the elastic modulus value, and presence of Mg^{2+} in the electrolyte decreases the elastic modulus of the collagen membrane.	123
A.4	Young's modulus values for the collagen membranes prepared with various concentrations of $CaCl_2$ and $Ca(NO_3)_2$. As with $CaCl_2$, the Young's modulus also increases with the concentration of $Ca(NO_3)_2$, which suggests that the cation Ca^{2+} plays a role in increasing the Young's modulus value, not the anion Cl^- . In fact, the nitrate salt increases the stiffness further because its additional electrochemical activity accelerates pH gradient formation.	124
B.1	Raman spectra for layered calcium-phosphate composites prepared from one of three different phosphate salts (K_2HPO_4 , KH_2PO_4 , or $NH_4H_2PO_4$) and (a) 10 mM $CaCl_2$ or (b) 10 mM $Ca(NO_3)_2$. Peaks indicative of hydroxyapatite (labeled HAp) and collagen (labeled fibril or monomer) are evident in all samples, except the one that is prepared with $CaCl_2$ and $NH_4H_2PO_4$, in which the obtained mineral phase is brushite. Spectra are offset along the intensity axis for clarity, and peak assignments are based on previous studies. ³⁻⁵	127

- B.2 Energy Dispersive X-ray spectra (EDX) of (a) collagen-hydroxyapatite and (b) collagen-brushite membranes. The EDX spectrum of this collagen-hydroxyapatite membrane has a ratio between the intensities of Ca and P peaks of 1.6, which is consistent with hydroxyapatite ($\text{Ca}_{10}(\text{PO}_4)_6(\text{OH})_2$). The Ca:P intensity ratio for a collagen-brushite membrane is 0.9, which is consistent with brushite ($\text{CaHPO}_4 \cdot 2\text{H}_2\text{O}$). . . 128
- B.3 Scanning Electron Microscope (SEM) images of collagen-hydroxyapatite and collagen-brushite membranes. (a) SEM image of a collagen-hydroxyapatite membrane shows that the hydroxyapatite crystals are well settled over the collagen membrane, and the collagen membrane is not visible because it is in the underneath of hydroxyapatite crystals. (b) SEM image of a collagen-brushite membrane shows that the brushite is settled over the collagen membrane, and the membrane folds are clearly visible. . . 129
- B.4 Atomic Force Microscope (AFM) images of collagen-hydroxyapatite and collagen-brushite membranes. (a) AFM image of a collagen-hydroxyapatite membrane shows crystals over the collagen membrane, and the collagen membrane is not visible because it is underneath. (b) AFM image of a collagen-brushite membrane shows that the brushite is settled over the collagen membrane, and the membrane fibrils are clearly visible. . . 129

Chapter 1

Introduction to collagen and collagen-calcium phosphate materials

In recent years, researchers have shown much interest in collagen and collagen-based materials for developing many artificial implant/repair materials like artificial bone, corneas, wound-care tissue, dermis and arterial replacement tissues.¹⁻⁶ Collagen is a family of proteins that accounts for $\sim 75\%$ of protein content in the whole body.⁷ It is abundant in fibrous tissues like skin and tendons and also a major component in blood vessels and the cornea.⁸ More than 90% of the organic matrix of bone is made up of collagen.⁹ The central layer of the cornea – the stroma – is made up of collagen,¹⁰⁻¹² and collagen is also present in the lens in a crystalline form.¹³ Collagen is also used as an extracellular matrix for many cell culture studies to assess how different kinds of cells interact with the microenvironments surrounding them during growth and development.¹⁴ Therefore, there is a great need for the development of new collagen based biocompatible materials for tissue repair and replacement that

can have a positive interaction with the host tissue.

1.1 Collagen

Collagen is comprised of three left handed helical polypeptide strands that coil together to form the right handed helix structure of collagen.¹⁵ Though there are 28 types of collagens found in nature, the type I, II, III and IV collagens constitute more than 90% of all collagen.^{16, 17} The classification of collagen is based on its α -chain. In type I collagen, two of the three α -chains have an identical sequence and the other chain has a different sequence.¹⁸ Collagen is a structural protein: the high strength of muscle tissues and the elasticity of skin are mainly due to collagen, and the degradation of collagen can damage the tissues or cause skin wrinkling.^{19, 20} The tissue strength largely depends on the way in which collagen molecules are crosslinked into thick fibrils.^{21, 22} Crystalline textured collagen is present in the cornea, where the uniformly gathered collagen fibrils assemble in an orthogonal lattice to maintain its high optical clarity.^{13, 23-25}

1.1.1 Structure of collagen

In collagen, three left-handed helical polypeptide strands coil together to form a right handed triple helix tropocollagen. In the polypeptide chain, there are 3.33 amino acid residues per helix turn, and there are ~ 1000 residues per chain. The helix diameter is 1.5 nm and the length is 300 nm.²⁶ In general, the repeated sequence of the amino acids in the collagen polypeptide strand is



where Gly is glycine and any amino acid can replace the Xaa and Yaa positions. $-\text{Gly} - \text{Pro} - \text{Hpro} -$ is the most common and most stable sequence in which Pro and

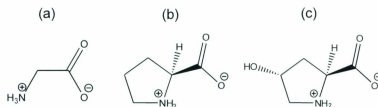


Figure 1.1: Zwitterionic structures of (a) glycine, (b) *L*-proline and (c) *trans*-4-hydroxy-*L*-proline.

Hpro are the aminoacids proline and hydroxyproline.²⁷ The zwitterionic structures of glycine, proline and hydroxyproline amino acids are given in Figure 1.1. It is mandatory to have the amino acid glycine at every third position in the helical portion of the protein. To have a higher packing density, glycine always occupies the middle of the triple helix so that the bulky side chains of other amino acids are placed outside.²⁸ This is because glycine is the smallest amino acid, and its presence at every third position makes the strand more flexible to coil in a helical structure. The presence of hydrogen bonds between the strands further stabilizes the collagen triple helix.²⁹ Any mutation that replaces glycine affects the molecular structure thus leading to disease.³⁰

1.1.2 Hierarchical assembly of collagen

The hierarchical assembly of collagen molecules into collagen fibers occurs via a highly complex mechanism and involves several steps (Figure 1.2).^{26, 31-35} During the biosynthesis of collagen fibrils, the collagen genes form procollagen, a helical protein strand. The two termini of this peptide strand are formed by two small peptide chains, called N-and C-propeptides. Three procollagen strands gather together into

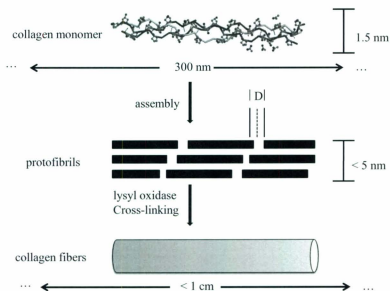


Figure 1.2: Schematic diagram for the hierarchical assembly of collagen fiber from collagen monomer. Image is modified from Reference [31].

a triple helix structure called procollagen, in the presence of lysyl hydroxylase and protein disulfide-isomerase enzymes. In procollagen processing, the procollagen N- and C-proteinases cleave the N- and C-terminal propeptides from the procollagen to give a tropocollagen triple helix. The diameter of this tropocollagen is 1.2 nm, the length is ≤ 300 nm and the two new termini are called N- and C- telopeptides. After that, numerous tropocollagen molecules assemble into a staggered configuration to give a collagen microfibril, with the molecular axes of the tropocollagen molecules parallel to the axis of collagen microfibril. These microfibrils can present banding of various periodicities, with the "native type fibril" showing a periodicity of about 67 nm ("D banding").^{23, 36, 37} The thickness of this collagen microfibril is ~ 5 nm, and in the presence of lysyl oxidase, cross-linking of several microfibrils takes place to give a ~ 500 nm thick, ~ 1 cm long collagen fiber.

1.1.3 *In vitro* collagen assembly methods

In the laboratory, there are numerous ways to align collagen molecules to form a membrane.³⁸ A few selected examples are discussed as follows.

1.1.3.1 Magnetic alignment

The assembly of collagen molecules into a membrane can be done using magnets because the magnetic field does not destroy the biological structures.³⁹ In the magnetic alignment method, the fibrillogenesis of collagen monomers into highly aligned collagen fibrils is performed by exposing a heated monomer solution to a strong magnetic field. The membranes obtained by this method have very high orientational alignment. This method needs a very high magnetic field strength in the range of 1 to 6 Tesla. Using a Tesla power magnet to prepare a membrane few cm^2 in size requires a large initial investment.

1.1.3.2 Electro-spinning process

Electro-spinning methods are also used to coat the collagen fibers on a substrate.⁴⁰ In the electro-spinning process, collagen monomers are taken up in a syringe pump that is connected to the positive lead of a high voltage power source. A cylindrical shaped target metal is connected to the negative lead of the power source. During the electro-spinning process, the syringe pump delivers the ionized collagen, and this collagen assembles well over the rotating substrate. The structural and mechanical properties (such as stiffness) of the formed collagen membrane can be altered by changing the type or the concentration of the collagen solution. However, the need of a cylindrical shaped substrate and the usage of corrosive and toxic chemicals as solvents make this method unsuitable for many applications.

1.1.3.3 Liquid crystalline ordering

In liquid crystalline ordering, evaporation is used to align collagen fibers in a specific manner.^{41, 42} Highly concentrated procollagen monomer solution (5 mg/mL to 30 mg/mL) is placed on a glass slide, which is covered by a cover slip. Three sides of the glass slide are sealed by epoxy, and the slide is kept in a moisture chamber that is maintained at 4–6 °C to control the evaporation. After a few days, the procollagen molecules assemble to form a liquid crystalline structure, and it can take several weeks to months to get a higher order crystalline texture.

1.1.3.4 Microfluidic alignment

Microfluidic alignment can be used to orient collagen fibers in three dimensions.⁴³ In this method, channels that are made from polydimethylsiloxane (PDMS) are widely used for the collagen fibrillogenesis. These PDMS channels are filled with collagen monomers either with flow or without flow assistance, and the collagen monomers are

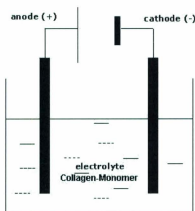


Figure 1.3: Schematic diagram of a two-electrode electrochemical cell. A collagen monomer solution is used as the electrolyte, and two polished stainless steel plates are used as electrodes. Once potential is applied to the collagen electrolyte, a highly aligned, mechanically robust collagen membrane can form parallel to the anode and cathode.

allowed to polymerize in the channels. Though this method is very simple and cost effective, the obtained membrane is very small in size (thickness of a few nanometers) and lacks a three dimensional hierarchical structure.

1.1.3.5 Electrochemical aggregation

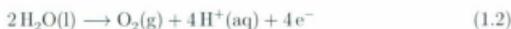
Since all of the above mentioned methods have some drawbacks, it is necessary to have an alternative method for collagen membrane formation that is simple, cost effective, and produces membranes with good orientational and mechanical properties.

In 1964, Becker *et al.* found that when a collagen monomer solution is placed in an electric potential (Figure 1.3), a band of collagen fibers is formed perpendicular to the

direction of current flow, and unlike the normal electrochemical deposition process, the formed collagen band is at a definite distance from the cathode.⁴⁴ Initially, these electrochemically prepared membranes did not show higher orientational anisotropy and D-banding, resulting in poor mechanical strength and packing density.⁴⁵ Changing key electrochemical parameters such as voltage and current did not yield better results. Later, it was found that changing other electrochemical parameters like electrochemical cell dimension and electrolyte composition could yield mechanically robust collagen bundles with higher orientational anisotropy.³⁸

1.1.4 Mechanism of electrochemical collagen membrane formation

The electrochemical formation of a collagen membrane is result of the following two reactions that occur at the cathode (Equation 1.1) and anode (Equation 1.2) when a potential is applied between the electrodes.



These two reactions occur when the applied electrode potential is much larger than the water electrolysis threshold voltage (1.23 V versus standard hydrogen reference electrode). These two electrochemical reactions play a vital role in forming a pH gradient in the electrolyte solution. Due to these redox reactions, the pH of the collagen electrolyte near the cathode increases (because of the consumption of H^+ ions) and the pH near the anode decreases (because of the formation of H^+ ions).

The aggregation of collagen monomer molecules into a thin, robust membrane can be explained by a mechanism called iso-electric focusing. Because of its amphoteric

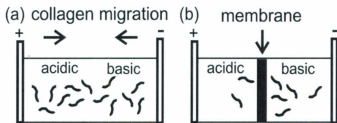


Figure 1.4: Schematic of the electrochemical membrane formation process. (a) Collagen molecules in the acidic side get a negative charge and the molecules in the basic side gain a positive charge due to the pH gradient. (b) A collagen membrane forms by migration of collagen monomers driven by an applied field between the two electrodes.

nature, the collagen molecules have both positively and negatively charged groups. As soon as the surrounding pH changes due to the pH gradient, the collagen molecules get a negative or positive charge by losing or gaining a proton (H^+). When the environmental pH is lower than the iso-electric point of collagen (which is ~ 6.5 for our collagen^{46, 47}), the collagen molecules become positively charged; for higher pH (> 6.5) the collagen molecules become negatively charged. When the environmental pH equals the iso-electric point, the collagen molecules do not carry a net charge.

Once the applied potential generates a pH gradient in the electrochemical cell, the positively charged collagen molecules in the anode side move toward the cathode, and the negatively charged collagen molecules in the cathode side move toward the anode. These collagen molecules assemble as a membrane at the point in the electrochemical cell where the pH is ~ 6.5 (Figure 1.4).^{46, 48}

After the electrochemical aggregation process, the electrolyte in the cathode region ($pH \sim 12$) is more viscous than in the anode region ($pH \sim 4$). This is because the

collagen molecules assemble more readily in basic environment resulting in higher fibril content in the cathode side of the cell.⁴⁹

1.1.5 Atomic force microscopy for imaging collagen

Earlier research in imaging collagen and other biomaterials was based on electron microscopy and histological staining to enhance the contrast in optical microscopy.⁵⁰⁻⁵² Though these methods give some information about the morphology and structured layers of biomaterials, they are not ideal for imaging most biological samples including collagen.⁵³ The maximum resolution that can be obtained using optical microscopy is $1\ \mu\text{m}$, and the depth of field is very low. Highly transparent samples cannot be viewed using optical microscopes without staining for better optical contrast. Fluorescent microscopy needs the sample to be fixed with dyes or tagged with some fluorescent particles for a clear view. For scanning electron microscopy (SEM), though a resolution of $5\ \text{nm}$ can be reached with a large depth of field, the sample needs to be stable in vacuum and must be coated with a conductive layer. Although an environmental SEM does not need the sample to be under vacuum, the sample must still be coated with a conductive layer for obtaining a higher resolution image. By doing any of the above, the biological sample is incorporated with artificial material and loses its original *in vivo* state when it is ready for imaging. All the microscopies mentioned above provide two dimensional data of optical or electron density.

On the other hand, atomic force microscopy (AFM) provides very high resolution 3D (x , y and z) images for many biological samples in a condition that can be made similar to the biological *in vivo* environment. The resolution of AFM can reach up to $0.1\ \text{nm}$ in the xy (sample) plane and up to $0.01\ \text{nm}$ in the z direction, depending on the quality of sample and as well as the quality of the tip.⁵⁴ AFM does not require the sample to be kept under vacuum and provides the images with very little or no

sample preparation.

In AFM, a micron sized cantilever tip moves across the sample surface, and the deflection in the cantilever due to the surface morphology of the sample is detected by a laser beam, which is reflected from the cantilever surface. The change in the deflection of the cantilever is converted into the topography of the sample. In addition to getting the topographical images, AFM can also be used to acquire the physicochemical and mechanical (stiffness and modulus) properties of the sample.^{53, 55} With all of these advantages, AFM has become an important tool for imaging and assessing the surface and internal properties of samples in many fields, including chemistry, biology, physics and materials science.^{54, 56, 57}

AFM has been widely used for understanding the assembly,^{58, 59} morphological structure and mechanical properties of collagen membranes. Habelitz *et al.*⁶⁰ have used AFM for imaging partially demineralized human dentin collagen fibrils *in situ* in three dimensions. The effect of hydration on the structural properties of the mineralized collagen has been revealed by obtaining high resolution AFM images of hydrated and dehydrated mineralized collagen fibrils. These images clearly show the *D*-banding of collagen fibrils and that the fibrils get thicker when they are hydrated. AFM has been also used to find the collagen fiber structure, and the results are consistent with the structure of collagen obtained from X-ray diffraction (XRD) and electron microscopy.⁶¹ The size of gap and overlap zones have been measured precisely using AFM because of its very high resolution in the *z* direction.

The mechanical properties of collagen membranes and collagen-based biomaterials have been widely studied using AFM. Graham⁶² has used AFM for studying the effect of disease on the mechanics of a collagen membrane. The mechanical properties of normal type I collagen and osteogenesis imperfecta (brittle bone disease) collagen were studied, and compared to assess how a disease affects the mechanical strength

of the collagen. Moreover, the change in the mechanics of collagen membrane during the cell interaction has also been studied using AFM. An AFM nanoindentation technique has been used by Wenger *et al.*⁶³ to optimize the mechanical properties of collagen fibrils. In their work, a single collagen fibril was laid down on a stiff substrate, and the nanoindentation was carried out over the fibril to acquire the force *vs.* displacement plots. Using appropriate models, the stiffness and elastic modulus of rat tail type I collagen fibril were calculated. Also, others have used AFM nanoindentation to find the mechanical properties of individual collagen fibrils, fibers, gels and membranes.⁶⁴⁻⁶⁶

1.2 Bone implants based on collagen-calcium phosphate composites *

Natural bone is a complex and hierarchically structured composite material based on collagen, hydroxyapatite (HAp), $\text{Ca}_{10}(\text{PO}_4)_6(\text{OH})_2$, with magnesium and carbonate ion substitutions. The distinctive combination of strength and light weight that is ascribed to bone comes not from the inherent strength of the composite, but rather from the way the composite material is structured.^{67, 68} Structure and strength are intimately related to the presence of collagen (type I), and other organic components.⁶⁹ It is interesting that, although there are many different phases of calcium phosphate (Table 1.1), only apatitic phases are found in bone.^{67, 70}

There have been many studies that have focused on nucleation and crystallization of bone-like apatitic minerals.⁷⁰⁻⁷⁴ However, there is still much to be investigated (and

*Modified from "A Role for Electrochemical Synthesis in Bioceramic Composite Materials" M. Ramesh Kumar, Erika F. Merschrod S., Kristin M. Poduska, *Ceramic Transactions* **2011**, 218 3-13. The candidate contributed to experimental design, collected and analyzed all data, and contributed to the revision of the manuscript.

Table 1.1: Selected calcium phosphate phases

Mineral name	Abbreviation	Composition
hydroxyapatite	HAp	$\text{Ca}_{10}(\text{PO}_4)_6(\text{OH})_2$
dahlite		$\text{CaCO}_3 \cdot 2 \text{Ca}_3(\text{PO}_4)_2$
brushite		$\text{CaHPO}_4 \cdot 2\text{H}_2\text{O}$
monetite		CaHPO_4
octacalcium phosphate	OCP	$\text{Ca}_8(\text{HPO}_4)_2(\text{PO}_4)_4 \cdot 5\text{H}_2\text{O}$
tricalcium phosphate	TCP	$\text{Ca}_3(\text{PO}_4)_2$
amorphous calcium phosphate	ACP	$\text{Ca}_x(\text{PO}_4)_y \cdot z\text{H}_2\text{O}$

understood) in terms of how the mesoscale structure and properties of bone relate to bone regeneration, in both natural and artificial environments.⁷⁵⁻⁷⁸

1.2.1 Target properties for effective bone implants and coatings

The role of an implant coating is to increase the likelihood that the implant is seamlessly incorporated into the body.^{79, 80} Clinical studies have shown that calcium phosphate-based coatings dramatically accelerate the body's incorporation of metal pins.⁸¹ An approach to improving the bioactivity of an implant coating is to embed specific incorporants in a composite to tailor the interaction between the implant and the body.^{76, 82, 83} For example, since natural bone contains both mineral and proteinaceous components, it may be desirable to incorporate proteins such as collagen into calcium phosphate based implant coatings; this has been addressed with theoretical⁸⁴

and experimental^{68, 85} studies.

Though many implant coatings are based on amorphous calcium phosphate, it is not yet clear whether specific calcium phosphate phases present advantages (or disadvantages) in terms of implant coating performance.⁸⁶ As the bone growth occurs, the interactions between cells and the implant can be affected by the topographic cues on the coating.^{76, 78, 87}

1.2.2 Overview of synthesis methods for bone implants and coatings

Developing an implant coating for which one can control the attributes described above is a challenge. The synthesis of these coatings often involves multiple steps, each of which can be grouped into one of three broad categories. For the most part, these syntheses produce stoichiometric calcium phosphates (HAp, brushite, OCP, or TCP) with collagen or collagen-carbonated apatites. There are a number of recent reviews focused on biomineral synthesis, both stoichiometric and substituted.^{70, 82, 88}

1.2.2.1 Thermal synthesis

Hydrothermal, spray pyrolysis, and conventional high-temperature treatments have all been used to make bone-like implant coatings.⁸⁸ These offer the possibility of thermodynamic selectivity of different calcium phosphate phases, as well as the option of controlling crystallite size and uniformity. An alternative approach is to chemically dissolve or mechanically grind natural bone into small particles, to then be coated onto a substrate and heat treated for optimal adherence.⁸⁹

Other thermal studies have used high temperature processes to control morphology as well as composition. Micrometer-scale bubbles have been used to induce bone-like porosity into the composite materials, and sacrificial incorporants that can be

thermally removed by combustion have also been used to create porous structures.⁷⁴ Since many organic or pharmaceutical additives are not stable at the high temperatures used in these thermal synthesis techniques, such incorporants are typically added in a separate, low-temperature step as a top layer to the implant coating.

1.2.2.2 Solution-phase synthesis

Given that bones can grow in the body at relatively low temperatures (37 °C), some methods are meant to mimic the body's growth environment through the use of biological molecules used by cells to stimulate and organize the mineralization process.^{74, 90} Others are designed to use chemistry that is very different from what takes place in the body, such as the use of alkaline treatments to control phase selectivity.⁸⁸ Because alkaline treatments can cause denaturation of protein incorporants, multi-step coating preparation processes are often employed.

1.2.2.3 Electrochemically assisted synthesis

An extension of the chemical methods for collagen-calcium phosphate crystallization involves the use of an applied electric potential to trigger an electrochemical crystallization reaction. This kind of hydrolysis-induced precipitation reaction is well-known.^{72, 91-93} Electrodeposition offers the option of using applied potential to control the energetics of the reaction without need for high temperatures. Therefore, it provides the possibility of controlling both kinetics and thermodynamics in a single, low-temperature reaction process.

Electrodeposition presents both advantages and limitations. The electrochemical precipitation process occurs only in the immediate vicinity of the substrate (working electrode) surfaces. This means that in general, electrically conductive substrates are required. For metal bone pins and similar stainless-steel or titanium alloy implants,

this is not a problem. In fact, electrodeposition offers the capability of coating complex electrode shapes due to the conformal nature of the electrodeposit. There are several examples of phase-selective materials synthesis procedures using electrochemical methods.^{73, 93, 94}

1.2.3 Electrochemically prepared biominerals

With many crystalline phases of calcium phosphate minerals known to exist, we sought a method to selectively form specific calcium phosphate phases. We use electrochemical hydrolysis to create a spatially localized *pH* change in the electrolyte where the alkaline *pH* conditions trigger a calcium phosphate precipitation process. This mechanism has been used extensively to synthesize calcium phosphate coatings.^{2, 72, 95, 96} Moreover, the electrosynthesis conditions (more specifically, the buffering capacity of the electrolyte) can be used to selectively produce two different calcium phosphate phases in a one-step deposition process, without the need for alkaline or high-temperature treatments.⁷³

The key to this control is evident upon closer analysis of the chemistry involved in the deposition procedure. The electrochemically assisted precipitation of HAP requires an alkaline environment. This ensures that the increased OH^- concentration is spatially confined to the working electrode surface, preventing precipitation from the bulk electrolyte. Equation 1.3 shows the reduction reaction of NO_3^- to NO_2^- in the presence of H_2O (-0.23 V *vs.* SCE⁷³). The OH^- ions from Equation 1.3 react with the H_2PO_4^- to give HPO_4^{2-} (Equation 1.4). Hydroxyapatite ($\text{Ca}_{10}(\text{PO}_4)_6(\text{OH})_2$) is obtained when HPO_4^{2-} reacts with Ca^{2+} and OH^- (Equation 1.5).





When there is insufficient OH^- present, brushite forms at the expense of HAp. This work demonstrates that a simple way to control the amount of OH^- present is to adjust the buffering capacity of the electrolyte through changing hydrogen phosphate concentration.⁷³

1.3 Overview of the thesis

In this thesis, I have used an electrochemical method to aggregate collagen monomers into collagen fibrils. Investigations were carried out to find out the effects of electrolyte composition on the structural and mechanical properties of the synthesized collagen membranes (Chapter 2). Collagen-calcium phosphate membranes were prepared by an electrochemical method, in which the collagen fibrils were assembled in aqueous solutions and the calcium phosphate minerals were precipitated over them. Various techniques were used to analyze the internal structure, composition and phase of the collagen-mineral composites (Chapter 3). Biocompatibility tests (based on observations of cell attachment and growth) and development of an artificial cornea using electrochemically aggregated collagen as a matrix have been carried out in collaboration with Drs. Robert Gendron and H el ene Paradis at the School of Medicine, MUN (Chapter 4). To understand the size and structure of the pores in the collagen membranes, a widely employed single particle tracking (SPT) method has been used. SPT experiments have also been used to relate the internal pore structure with the stiffness of collagen membranes (Chapter 5).

References

- [1] Giusti, P.; Lazzeri, L.; De-Petris, S.; Palla, M.; Cascone, M. G. *Biomaterials* **1994**, *15*, 1229–1233.
- [2] Fan, Y.; Duan, K.; Wang, R. *Biomaterials* **2005**, *26*, 1623–1632.
- [3] Miyashita, H.; Shimmura, S.; Kobayashi, H.; Taguchi, T.; Asano-Kato, N.; Uchino, Y.; Kato, M.; Shimazaki, J.; Tanaka, J.; K, T. *J. Biomed. Mater. Res. B. Appl. Biomater.* **2006**, *76*, 56–63.
- [4] Vrana, E. N.; Builles, N.; Justin, V.; Bednarz, J.; Pellegrini, G.; Ferrari, B.; Damour, O.; Hulmes, D. J. S.; Hasirci, V. *Invest. Ophthalmol. Vis. Sci.* **2008**, *49*, 5325–5331.
- [5] Vescovali, C.; Damour, O.; Shahabedin, L.; David, M. F.; Dantzer, E.; Marichy, J.; Collombel, C.; Echinard, C. *Annals of the BBC* **1989**, *2*, 3.
- [6] Daly, C. D.; Campbell, Gordon. R Walker, P. J.; Campbell, J. H. *Expert. Rev. Cardiovasc. Ther.* **2005**, *3*, 659–665.
- [7] Di Lullo, G. A.; Sweeney, S. M.; Korkko, J.; Leena, A.-K.; . San Antonio, J. D. *J. Biol. Chem.* **2002**, *277*, 4223–4231.
- [8] Popo, T. *Characterization of human mesenchymal stem cells by the appearance of integrins and functional analysis of collagen I-binding integrins*, Thesis, University of Munich, 2011.
- [9] Paschalis, E. P.; Verdels, K.; Doty, S. B.; Boskey, A. L.; Mendelsohn, R.; Yamauchi, M. *J. Bone Miner. Res.* **2001**, *16*, 1821–1828.
- [10] Leonard, D. W.; Mee, K. M. *Biophys. J* **1997**, *72*, 1382–1387.

- [11] Dische, Z.; Cremer-Bartels, G.; Kaye, G. I. *Proc. Natl. Acad. Sci. USA* **1985**, *82*, 760–764.
- [12] Kannabiran, C. *J. Genet.* **2009**, *88*, 487–494.
- [13] Clark, J. I. *Exp. Eye. Res.* **2004**, *78*, 427–432.
- [14] Blow, N. *Nature Methods* **2009**, *6*, 619–622.
- [15] Fields, G. B.; Prockop, D. J. *Biopolymers (Pept. Sci.)*. **1996**, *40*, 345–357.
- [16] Veit, G.; Kobbe, B.; Keene, D. R.; Paulsson, M.; Koch, M.; Wagene, R. *J. Biol. Chem* **2006**, *281*, 3494–3504.
- [17] Canty, E. G.; Kadler, K. E. *J. Cell. Sci.* **2005**, *118*, 1341–1353.
- [18] Gordon, M. K.; Hahn, R. A. *Cell. Tissue. Res.* **2010**, *339*, 247–257.
- [19] Elfrich, Y.; Sachs, D.; Voorhees, J. *Dermatol. Nurs.* **2008**, *20*, 177–183.
- [20] Rijken, F.; Bruijnzeel, P. L. B. *J. Invest. Derm. Symp. P* **2009**, *14*, 67–72.
- [21] Silver, F. H.; Freeman, J. W.; Seehra, G. P. *J. Biomech.* **2003**, *36*, 1529–1553.
- [22] Eyre, D. R.; Wu, J.-J. *Top. Curr. Chem.* **2005**, *247*, 207–229.
- [23] Holmes, D. F.; Gilpin, C. J.; Baldock, C.; Ziese, U.; Koster, A. J.; Kadler, K. E. *Proc. Natl. Acad. Sci. U. S. A* **2001**, *98*, 7307–7312.
- [24] Ruggiero, F.; Burillon, C.; Garrone, R. *Invest. Ophthalmol. Vis. Sci.* **1996**, *37*, 1749–1760.
- [25] Li, S.; Diepstraten, C. V. D.; D'Souza, S. J.; Chan, B. M. C.; Pickering, J. G. *Am J Pathol* **2003**, *163*, 1045–1056.

- [26] Gautieri, A.; Vesentini, S.; Redaelli, A.; Buehler, M. J. *Nano. Lett.* **2011**, *11*, 757–76.
- [27] Ramshaw, J. A. M.; Shah, N. K.; Brodsky, B. *J. Struct. Biol.* **1998**, *122*, 86–91.
- [28] Gelse, K.; Pöschl, E.; Aigner, T. *Adv. Drug. Deliv. Rev.* **2003**, *55*, 1531–1546.
- [29] Bella, J.; Berman, H. M. *J. Mol. Biol.* **1996**, *264*, 732–742.
- [30] Persikov, A.; Pillitteri, R.; Amin, P.; Schwarze, U.; Byers, P.; Brodsky, B. *Hum. Mutat* **2004**, *24*, 330–337.
- [31] Shoulders, M. D.; Raines, R. T. *Annu. Rev. Biochem.* **2009**, *78*, 929–958.
- [32] Kadler, K.; Holmes, D.; Trotter, J.; Chapman, J. *Biochem J* **1996**, *316*(Pt 1), 1–11.
- [33] Prockop, D. J.; Fertala, A. *J. Struct. Biol.* **1998**, *122*, 111–118.
- [34] Orgel, J. P.; Miller, A.; Irving, T. C.; Fischetti, R. F.; Hammersley, A. P.; Wess, T. J. *Structure.* **2001**, *9*, 1061–1069.
- [35] Buehler, M. J. *Proc. Natl. Acad. Sci. USA* **2006**, *103*, 12285–12290.
- [36] Ortolani, F.; Giordano, M.; Marchini, M. *Biopolymers.* **2000**, *54*, 448–463.
- [37] Lingham-Soliar, T.; Wesley-Smith, J. *Proc. R. Soc. B.* **2008**, *275*, 2207–2212.
- [38] Cheng, X.; Gurkan, U. A.; Dehen, C. J.; Tate, M. P.; Hillhouse, H. W.; Simpson, G. J.; Akkus, O. *Biomaterials* **2008**, *29*, 3278–3288.
- [39] Torbet, J.; Ronzière, M. C. *Biochem. J.* **1984**, *219*, 1057–1059.
- [40] Matthews, J. A.; Wnek, G. E.; David G. Simpson, D. G.; Bowlin, G. L. *Biomacromolecules* **2002**, *3*, 232–238.

- [41] Martin, R.; Farjanel, J.; Eichenberger, D.; Colige, A.; Kessler, E.; Hulmes, D. J.; Giraud-Guille, M. M. *J. Mol Biol.* **2000**, *301*, 11–17.
- [42] Abu-Rub, M. T.; Billiar, K. L.; Van Es, Maarten, H.; Knight, A.; Rodriguez, B. J.; Zeugolis, Dimitrios, I.; McMahon, S.; Windebank, A. J.; Pandit, A. *Soft. Matter* **2011**, *7*, 2770–2781.
- [43] Lee, P.; Lin, R.; Moon, J.; Lee, L. P. *Biomed. Microdev.* **2006**, *8*, 35–41.
- [44] Pawluk, R. J.; Becker, R. O. *Nature (Lond.)* **1964**, *204*, 652–654.
- [45] Marino, A. A.; Becker, R. O. *Calc. Tiss. Res.* **1970**, *4*, 330–338.
- [46] Baker, H. R.; Merschrod S., E. F.; Poduska, K. M. *Langmuir* **2008**, *24*, 2970–2972.
- [47] Taylor, S. *Advances in Food and Nutrition Research*; Academic Press, Burlington, MA 01803, USA: 2010.
- [48] Kumar M, R.; Merschrod S., E. F.; Poduska, K. M. *Biomacromolecules* **2009**, *10*, 1970–1975.
- [49] Hayashi, T.; Nagai, Y. N. *J. Biochem* **1973**, *73*, 999–1006.
- [50] Tateya, T.; Tateya, L.; Bless, D. M. *Ann. Otol. Rhinol. Laryngol.* **2006**, *115*, 469–476.
- [51] Sato, K.; Hirano, M.; Nakashima, T. *Ann. Otol. Rhinol. Laryngol* **2002**, *111*, 15–20.
- [52] Sato, K. *Ann. Otol. Rhinol. Laryngol.* **1998**, *107*, 1023–1028.
- [53] Sivasankar, M.; Ivanisevic, A. *The Laryngoscope* **2009**, *117*, 1876–1881.

- [54] Blanchard, C. R. *The Chemical Educator*; Springer - Verlag Newyork, Inc: 1996.
- [55] Dupont-Gillain, C. C.; Rouxhet, P. G. *Langmuir* **2001**, *17*, 7261–7266.
- [56] Jandt, K. D. *Surf. Sci.* **2001**, *491*, 303–332.
- [57] Bolshakova, A. V.; Kiselyova, O. I.; Yaminsky, I. V. *Biotechnol. Prog.* **2004**, *20*, 1615–1622.
- [58] Paige, M. F.; Goh, M. C. *Micron* **2001**, *32*, 355–361.
- [59] Paige, M. F.; Goh, M. C. *Micron* **2001**, *32*, 341–353.
- [60] Habelitz, S.; Balooch, M.; Marshall, S. J.; Balooch, G.; Marshall, J. G. W. *J. Struct. Biol* **2002**, *138*, 227–236.
- [61] Revenko, I.; Sommer, F.; Minh, D. C.; Garrone, R.; Franc, J.-M. *Biol. Cell* **1994**, *80*, 67–69.
- [62] Graham, J. S. *Mechanical Properties of Complex Biological Systems using AFM-Based Force Spectroscopy*, Thesis, University of Missouri-Columbia, 2005.
- [63] Wenger, M. P. E.; Bozec, L.; Horton, M. A.; Mesquida, P. *Biophys. J.* **2007**, *93*, 1255-1263.
- [64] Yang, L. *Mechanical properties of collagen fibrils and elastic fibers explored by AFM*, Thesis, University of Twente, 2008.
- [65] Hang, F.; Lu, D.; Barber, A. H. *Mater. Res. Soc. Symp. Proc* **2009**, *1187*, 1187-KK06-06.
- [66] Dong, Z.; Wejinya, U. C.; Yanxia, Z.; Kaiming, Y. Force measurement study of engineered collagen-chitosan scaffold using Atomic Force Microscopy. In *IEEE-*

*Wiley eBooks Library, IBM Journal of Research and Development, VDE VER-
LAG Conference Proceedings*; 2010.

- [67] Weiner, S.; Wagner, H. D. *Annu. Rev. Mater. Sci.* **1998**, *28*, 271–298.
- [68] Palmer, L. C.; Newcomb, C. J.; Kaltz, S. R.; Spoerke, E. D.; Stupp, S. I. *Chem. Rev.* **2008**, *108*, 4754–4783.
- [69] Olszta, M. J.; Cheng, X.; Jee, S. S.; Kumar, R.; Kim, Y.-Y.; Kaufman, M. J.; Douglas, E. P.; Gower, L. B. *Mater. Sci. Engr. R* **2007**, *58*, 77–116.
- [70] Wang, L.; Nancollas, G. H. *Chem. Rev.* **2008**, *108*, 4628–4669.
- [71] Qiu, S. R.; Orme, C. A. *Chem. Rev.* **2008**, *108*, 4784–4822.
- [72] Zhitomirsky, I. *Adv. Colloid. Interface. Sci.* **2002**, *97*, 279–317.
- [73] Huelin, S. D.; Baker, H. R.; Merschrod S., E. F.; Poduska, K. M. *Crystal Growth & Design* **2006**, *6*, 2634–2636.
- [74] Meldrum, F. C.; Cölfen, H. *Chem. Rev.* **2008**, *108*, 4332–4432.
- [75] Davies, J. E. *Biomaterials* **2007**, *28*, 5058–5067.
- [76] Stevens, M. M.; George, J. H. *Science* **2005**, *310*, 1135–1138.
- [77] Boyan, B. D.; Lohmann, C. H.; Dean, D. D.; Sylvia, V. L.; Cochran, D. L.; Schwartz, Z. *Annu. Rev. Mater. Res.* **2001**, *31*, 357–371.
- [78] Barrère, F.; Mahmood, T.; de Groot, K.; van Blitterswijk, C. *Mater. Sci. Eng. R* **2008**, *59*, 38–71.
- [79] Sakiyama-Elbert, S. E.; Hubbell, J. A. *Annu. Rev. Mater. Res.* **2001**, *31*, 183–201.

- [80] Zapanta LeGeros, R. *Chem. Rev.* **2008**, *108*, 4742–4753.
- [81] Pichler, H. R. *MRS Bull.* **2000**, *25*, 67–70.
- [82] Best, S. M.; Porter, A. E.; Thian, E. S.; Huang, J. *J. Eur. Ceram. Soc.* **2008**, *28*, 1319–1327.
- [83] Williams, D. F. *Biomaterials* **2008**, *29*, 2941–2953.
- [84] Shen, J.-W.; Wu, T.; Wang, Q.; Pan, H.-H. *Biomaterials* **2008**, *29*, 513–532.
- [85] Cui, F.-Z.; Li, Y.; Ge, J. *Mater. Sci. Eng. R* **2007**, *57*, 1–27.
- [86] Gower, L. B. *Chem. Rev.* **2008**, *108*, 4551–4627.
- [87] Discher, D. E.; Janmey, P.; Wang, Y. L. *Science* **2005**, *310*, 1139–1143.
- [88] Gao, Y.; Koumoto, K. *Cryst. Growth. Des.* **2005**, *5*, 1983–2017.
- [89] Haberko, K.; Bučko, M. M.; Brzezińska-Miecznik, J.; Haberko, M.; Mozgawa, W.; Panz, T.; Pyda, A.; Zarębski, J. *J. Eur. Ceram. Soc.* **2006**, *26*, 537–542.
- [90] George, A.; Veis, A. *Chem. Rev.* **2008**, *108*, 4670–4693.
- [91] Switzer, J. A. *Am. Ceram. Soc. Bull.* **1987**, *66*, 1521–1524.
- [92] Therese, G. H. A.; Kamath, P. V. *Chem. Mater.* **2000**, *12*, 1195–1204.
- [93] Lincot, D. *Thin Solid Films* **2005**, *487*, 40–48.
- [94] Switzer, J. A.; Liu, R.; Bohannan, E. W.; Ernst, F. *J. Phys. Chem. B* **2002**, *106*, 12369–12372.
- [95] Shirkhanzadeh, M. *J. Mater. Sci.: Mater. Med.* **1998**, *9*, 67–72.

- [96] Therese, G. H. A.; Kamath, P. V.; Subbanna, G. N. *J. Mater. Chem.* **1998**, *8*, 405-408.

Chapter 2

Correlating mechanical properties with aggregation processes in electrochemically fabricated collagen membranes *

2.1 Introduction

Knowledge of the mechanical properties of biological tissues is instrumental in understanding how structure affects their function. Tendons, for example, are aligned collagen-based connective tissue whose elastic properties have been widely studied at macroscopic length scales.¹⁻³ However, mechanical property investigations at smaller length scales, relevant to the local environment experienced by a cell, require smaller

*This chapter was published as "Correlating Mechanical Properties with aggregation processes in electrochemically fabricated collagen membranes" M. Ramesh Kumar, Erika F. Merschrod S., Kristin M. Poduska, *Biomacromolecules* **2009**, *10* 1970-1975. Used with permission. The candidate contributed to experimental design, collected and analyzed all data, wrote the initial draft of the manuscript, and participated in manuscript revisions.

probes. Force-displacement curves obtained with atomic force microscopy (AFM) cantilevers, whose tips have radii of curvature on the order of tens of nanometers, can be used in conjunction with appropriate mathematical models to describe the tip-sample contact mechanics and to estimate the Young's modulus and other structural parameters in a range of materials.⁴ Here, we show that mechanical property data obtained from AFM force-displacement curves can be used to distinguish possible formation pathways of complex collagen assemblies.

Collagen is a structural protein whose mechanical properties are intimately related to the assembly and aggregation of its monomeric building blocks. Its hierarchical aggregation process, fibrillogenesis, is fundamental to the *in vivo* development of collagenous connective tissues.⁵ These fibrils and smaller protofibrils are structurally and mechanically distinct from the less stiff, non-specifically aggregated collagen that can form under some conditions, as presented schematically in Figure 2.1. Fortunately, fibril formation can be replicated in a laboratory environment,⁵ which can aid development of synthetic collagen-based scaffolds for tissue repair and regeneration applications.^{6,7} Strategies for developing such scaffolds require controlled collagen assembly for reliable function, including control over packing density, elastic deformability, and the final size of the construct. These factors can affect bioactivity through mechanical response, or as a result of bioavailability issues arising from the porosity of the material.

Collagen aggregation and fibrillogenesis have been directed *in vitro* by stimulating alignment prior to or during aggregation *via* fluid flow, mechanical extrusion, microfluidic channels, or anisotropic chemical nanopatterns.^{1,8-12} An alternative class of approaches for providing high orientational order and packing density involves manipulating the electrochemical environment of collagen molecules. Marino and Becker¹³ reported that the electrolysis of a collagen solution could induce the formation of

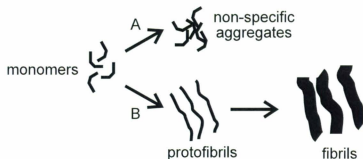


Figure 2.1: A schematic diagram of possible membrane formation pathways. Monomers can either aggregate (A) non-specifically or (B) hierarchically to form protofibrils (thickness of ~ 5 nm) and then fibrils (thickness of ~ 100 nm). Non-specific aggregates do not lead to fibril formation.

an opaque fibrous material, with aggregation induced by a local pH increase at the cathode. More recently, our group has reported the formation of macroscopic and microscopic 2D collagen membranes by a similar process,¹⁴ while others have made collagen bundles in the presence of electric fields^{3, 15}.

In this work, we demonstrate that AFM force measurements coupled with spectroscopic data allow us to understand how electrochemical synthesis parameters influence collagen membrane formation, toward the goal of a tailored membrane structure for scaffold applications. The Young's modulus changes that occur in our electrosynthesized membranes can be correlated directly with fibril content, but stiffness differences alone do not offer direct mechanistic information about the collagen aggregation process. Monitoring these Young's modulus changes in conjunction with local structure information from Raman scattering spectroscopy and morphological data from AFM images gives a more comprehensive picture of the relationship between membrane stiffness and collagen aggregation processes.

2.2 Experimental method

2.2.1 Sample preparation

Experiments were designed to investigate the effects of time, pH , and electrolyte composition on an electrochemically controlled collagen membrane formation process. The electrolyte contained collagen (Type I collagen monomers with a final concentration 0.07 mg/mL from 3 mg/mL acidic Vitrogen stock solution, Inamed Biomaterials), ultrapure water (18.2 M Ω -cm, Barnstead Nanopure), and sufficient NaOH (EMD Chemicals, ACS reagent grade) to reach pH 7, unless otherwise noted. Electrolytes more alkaline than pH 7 can lead to collagen denaturation, so this study focused on pH variations in the acidic regime. In some experiments, different concentrations (5-100 mM) of CaCl₂, KCl, and NaCl were added (at pH 7). All experiments were conducted at ambient temperature.

The electrochemically induced aggregation was carried out in a two-electrode electrochemical cell described in more detail elsewhere.¹⁴ A potential of 8 V (unreferenced) was applied with a potentiostat (Pine 366A) for durations of between 15 and 60 minutes. The resulting current data were recorded using a computer-based data acquisition program (National Instruments LabVIEW and NI-PCI 6014 digitizing board) with an interface designed in-house. The applied voltage was large relative to the potential required for hydrogen evolution, oxygen evolution, and oxygen reduction reactions. This led to H⁺ and OH⁻ generation at the anode and cathode, respectively, and results in a pH gradient. (Comparable results were observed with applied potentials referenced to a saturated calomel electrode.) Within minutes of exposing a pH -adjusted electrolyte of collagen monomers to the applied potential, isoelectric focusing in the pH gradient caused a collagen film to form perpendicular to the field, with its edges anchored to the container wall. Prior to subsequent measurements,

membranes were removed from the cell, rinsed with ultrapure water, and air-dried on a glass substrate under ambient conditions. Aliquots from the electrolyte were also collected, deposited on a glass substrate, and air-dried under ambient conditions. Variations in ambient humidity and temperature did not lead to statistically significant changes in membrane stiffness.

2.2.2 Optical characterization

The membrane formation process was monitored in real time during some experiments with a Leica DM2500 optical microscope and polarized light. Raman scattering spectroscopy (Jobin Yvon Horiba LabRAM, confocal, 532 nm excitation) on dried membranes tracked changes in intramolecular and intermolecular bonding, which are indicators for degree of collagen aggregation and/or denaturation. To assess how much of the collagen from the electrolyte was incorporated into the membrane, we used UV/Vis spectroscopy (Ocean Optics, Inc. Chem2000) on the post-deposition electrolyte to measure relative changes in absorption compared to an ultrapure water reference.

2.2.3 Atomic Force Microscopy

An atomic force microscope (MFP-3D AFM, Asylum Research) was used for thickness measurements, topographic mapping and force-displacement measurements. Experiments were performed at ambient temperature using silicon probes (MikroMasch NSC35) with spring constant ~ 17 nN/mm, as determined by the thermal noise method.¹⁶ Membrane thicknesses were assessed by AFM measurements at the edges of the samples, with measurement sites selected where the optical microscope indicated that the membrane was not folded over. Topographic images were acquired using tapping imaging mode at a scan rate of 0.5 Hz. Before beginning indentation measurements

on the sample, force curves were collected on a bare glass substrate to calibrate the deflection sensitivity of the instrument. Force curves were then collected at different locations on the collagen membrane within a $25 \mu\text{m}^2$ area, starting ~ 200 nm above the sample surface and indenting ~ 100 nm after initial contact with the sample. Force curve shape indicated that the measurements were not affected by the underlying substrate: the curvature of the extension and retraction curves was accounted for entirely by probe shape and did not show evidence of coupling with the harder substrate.⁴ These raw cantilever deflection voltage *vs.* probe displacement measurements were then converted into force-separation relations using the cantilever deflection sensitivities and the cantilever spring constants. We use a simplified model for the material response as purely elastic, neglecting any viscoelastic contributions and using only the retraction portion of the force-displacement curves to eliminate contributions from plastic deformation. Representative force curves and additional details on their analysis are provided in Section 2.3.

We note that the mechanical data were collected on dried membranes to avoid artifacts introduced by capillary forces. Force curves obtained on membranes that were never dried (or membranes that were rehydrated) are dominated by capillary forces, while measurements on dried membranes are free of these strong artifacts. Measurements on wet membranes conducted entirely under fluid present additional problems with inconsistent adhesion of the membrane to the underlying support, and with strong adhesion between tip and membrane. Membranes would likely be rehydrated when used in scaffolding applications, and this would change their Young's moduli. However, our interest here lies in using mechanical measurements to model the formation process of the membranes, and these data are obtained most consistently with dried membranes. We anticipate similar trends in Young's moduli when changing salt concentration for sets of wet membranes. We are interested in those trends, which can be

obtained from dried membranes much more easily, and the data from wet membranes would be unreliable.

2.2.4 Modeling stiffness

We employed two theoretical models that are widely used to extract Young's moduli. A hyperboloid tip shape¹⁷ is assumed in a Hertzian contact model,¹⁸ while the model of Oliver and Pharr^{19, 20} utilizes the shapes of retraction curves to determine effective indenter shape. By treating all data with both contact models, we confirmed that observed qualitative trends for changes in stiffness are not dependent on the specific details of the probe-sample contact modeling. Additional details and representative analyses from both models are included in Section 2.3.

2.2.4.1 Hertzian model

The force-indentation relation for a hyperboloidal contact¹⁷ is given by Equation 2.1

$$F = \frac{Ea^3}{(1-\sigma^2)R} \left[\xi^2 + (1-\xi^2) \frac{R\delta}{a^2} \right], \quad (2.1)$$

where F is the load force, ξ is $R \cot(\alpha)/a$, α is the tip conical angle (30° according to manufacturer specifications for our indenters), a is the contact area radius (calculated from tip shape and indentation depth), R is the probe's radius of curvature, E is the Young's modulus, σ is the sample's Poisson ratio (0.3 is a reasonable value for biological fibrils⁴), and δ is the indentation depth and is equal to

$$\delta = \frac{a^2 \xi}{2R} \left[\frac{\pi}{2} + \arctan \left(\frac{1}{2\xi} - \frac{\xi}{2} \right) \right] \quad (2.2)$$

An accurate calculation of the indentation depth δ would require precise knowledge of the probe-sample contact point. Instead, one can use an estimated tip-sample

separation⁴ (Δ) offset from the true indentation depth by a constant C : $\Delta = C - \delta$. It is then possible to rework Equation 2.1 so that the Young's modulus can be determined independently of the exact point of probe-sample contact.

2.2.4.2 Oliver-Pharr model

The Oliver-Pharr model^{20, 21} adopts a slightly more complex model for the indentation process. The effective Young's modulus E is related to the sample stiffness (S_{material}) and contact area (A) by

$$E = \frac{S_{\text{material}}}{2} \sqrt{\frac{\pi}{A}}, \quad (2.3)$$

when assuming an indenter that is approximately axially symmetric.¹⁹ The contact involves two springs connected in series: one for the AFM cantilever (spring constant K_c) and another for the sample (pseudo-spring constant S_{material}). These two spring constants are related to the slope of the force *vs.* indentation depth plot (S_{expt}) obtained from force curve measurements.

$$\frac{1}{S_{\text{material}}} = \frac{1}{S_{\text{expt}}} - \frac{1}{K_c} \quad (2.4)$$

The contact area A is determined by accounting for both the geometry of the tip and the plastic deformation from the extension process (which affects the tip-sample contact upon retraction). Fits of our retraction curves (described in Section 2.3) indicate that our contact area is effectively parabolic, so we use a contact area given by

$$A = 2 \pi R h_c - \pi h_c^2, \quad (2.5)$$

where R is the radius of curvature of the indenter and h_c is the contact depth.

The contact depth upon retraction is affected by plastic deformation from the exten-

sion process. If the sample is permanently indented during extension, the retraction process will occur over a shorter distance and will involve a different surface geometry and hence a different tip-surface contact. In principle, it would be possible to determine the retraction distance by measuring the height difference between the point of first tip-sample contact on the fresh sample (during the tip extension procedure) and the point of last tip-sample contact on the newly deformed sample (during the tip retraction procedure). However, adhesion effects could cause the height at which the tip disengages from the sample to be different from the true sample height. A solution that addresses the changes in both distance and shape during retraction estimates how much sinking deformation should occur to the sample²⁰ based on the maximum force applied during indentation F_{max} , the spring constant of the material being indented $S_{material}$, and the effective shape of the indenter ε .²¹ The true contact depth h_c is then the total measured height change h corrected for this sinking depth (Figure 2.2).

$$h_c = h - \left(\varepsilon \frac{F_{max}}{S_{material}} \right) \quad (2.6)$$

Each retraction curve is fitted (described in Section 2.3) to obtain ε , all of which are close to the 0.75 value of a paraboloid tip.²⁰ Since it is impractical to assess the radius of curvature for each indentation, our calculations are based on manufacturer specifications ($R = 20$ nm, MikroMasch, NSC 35). We note that variations in tip radius ± 10 nm lead to less than 10% change in the calculated Young's moduli.

2.3 Model force curve calculation

In this work, two common theoretical models (Hertzian contact, described recently in Reference [4] and Oliver-Pharr^{20, 21}) were used to find the Young's elastic modulus

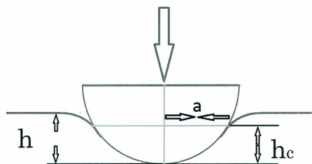


Figure 2.2: Schematic diagram of the nanoindentation process. a is contact area radius, h_c is true contact depth and h is measured depth. Image is modified from References [19, 20].

from atomic force microscopy (AFM) indentation curves. By showing that the stiffness trends yielded by both models are qualitatively and quantitatively similar, we demonstrate that the conclusions we draw from these stiffness data do not depend on the details of the probe-membrane contact models.

Deflection voltage *vs.* probe displacement data from AFM indentation measurements were converted into force-separation relations using the cantilever deflection sensitivities and the cantilever spring constant (~ 17 N/m). The same cantilever was used for all indentation measurements described here, and these results were verified by using other cantilevers with a similar range of spring constants (6-18 N/m).

A representative force curve, including extension and retraction, is shown in Figure 2.3a. The hysteresis between extension and retraction results from plastic deformation during the indentation (extension) process. Therefore, we used only the retraction curves to obtain information about the membranes' elastic properties.

One important difference between the Hertzian contact and Oliver-Pharr models is related to assessments of the true indentation depth. The Hertzian contact model uses an estimated tip-sample separation so that Young's modulus can be extracted from the plot's slope without precise determination of the tip-sample contact point. (This methodology is described in more detail in Reference [4].) Representative data from Hertzian contact modeling of force-displacement curves using a hyperboloidal indenter (as described in Reference [17]) are shown in Table 2.1. The normalized contact area radius ξ and indentation depth δ are calculated for each retraction curve.

In contrast to the hyperboloidal indenter assumed in our implementation of the Hertzian contact model, the Oliver-Pharr model defines the true contact depth into the sample in terms of the effective shape of the indenter (based on a fit of the retraction curve) and how much deformation occurs during the extension process. In principle, it would be possible to determine the true indentation depth by measuring

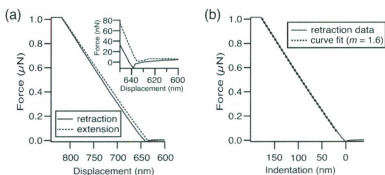


Figure 2.3: (a) A representative force-displacement curve obtained on a collagen membrane prepared from pH 7 electrolyte using 30 minutes of applied voltage. The dashed line is the extension curve, and the solid line is the retraction curve. The inset highlights the hysteresis between extension and retraction at the first and last points of probe-membrane contact. (b) Fitting the retraction curve to a power law expression yields a power coefficient $m = 1.6 \pm 0.1$, which is appropriate for a paraboloid indenter.

Table 2.1: Representative Young's moduli (E) extracted from the slopes of force-displacement data using the Hertzian contact model for a collagen membrane prepared from pH 7 electrolyte using 30 minutes of applied voltage.

Force Curve	ξ	δ (nm)	E (10^8 Pa)
1	0.33	229	1.04
2	0.36	202	1.28
3	0.33	231	1.04
4	0.33	229	1.06
5	0.35	211	1.20
6	0.34	220	1.15
7	0.33	228	1.07
8	0.34	218	1.16
9	0.34	218	1.17
10	0.34	219	1.17
Average	0.34 ± 0.03	220 ± 20	1.1 ± 0.1

the height difference between the point of first tip-sample contact on the fresh sample (during the tip extension procedure) and the point of last tip-sample contact on the newly deformed sample (during the tip retraction procedure). However, adhesion effects and plastic deformation could cause the height at which the probe disengages from the sample to be different from the true sample height. This problem can be avoided by estimating the depth along which contact is made between the probe and sample²⁰ based on: the maximum force applied during indentation F_{max} , the spring constant of the material being indented $S_{material}$, and a parameter that defines the effective contact area of the indenter ε .²¹ The true maximum contact depth (h_c) is the total measured height change (h) corrected for this sinking depth.

$$h_c = h - \left(\varepsilon \frac{F_{max}}{S_{material}} \right) \quad (2.7)$$

Using the method described in Reference [21], we fit the curvature of the retraction curves to a power law to determine the most appropriate indenter shape. A representative fit is shown in Figure 2.3b. We find a power exponent $m = 1.6 \pm 0.1$ for our probes, and this value is more consistent with that expected for a paraboloid indenter ($m = 1.5$) rather than for conical ($m = 2$) or flat punch ($m = 1$) shapes.²¹ Additionally, these retraction data show no evidence of coupling between the membranes and the harder substrates on which they sit.

Applying the Oliver-Pharr model to the same ten force-displacement curves noted in Table 2.1, we find higher Young's moduli values, as shown in Table 2.2. Despite the quantitative difference, the stiffness trends as a function of ion concentration, electrolyte pH, and the duration applied electric field are qualitatively the same for both models. Therefore, we draw conclusions about membrane formation based on these data trends rather than on the absolute Young's moduli values.

Table 2.2: Representative Young's moduli and related parameters extracted from force curve data using the Oliver-Pharr model for collagen membranes prepared from pH 7 electrolyte using 30 minutes of applied voltage. For all curves, we use $\epsilon = 0.75$ for our paraboloid indenter, in accordance with References [20, 21], and a cantilever spring constant $K_C = 16.87$ N/m.

Curve	F_{max} nN	h_{max} nm	S_{Expt} N/m	S_{Mat} N/m	h_c nm	E $\times 10^8$ Pa
1	4301	211	23.7	58.7	156	2.11
2	4313	191	25.6	49.6	126	2.31
3	4343	212	24.3	55.4	154	2.01
4	4357	211	25.0	52.1	148	1.99
5	4328	197	25.4	50.4	133	2.19
6	4421	204	23.5	60.0	149	2.28
7	4386	211	22.7	66.1	161	2.30
8	4406	203	23.8	57.9	146	2.25
9	4473	203	33.5	34.0	104	2.01
10	4479	204	24.3	55.2	143	2.20
Average	4380 ± 60	205 ± 7	25.2 ± 2.9	53.9 ± 8.1	143 ± 16	2.16 ± 0.12

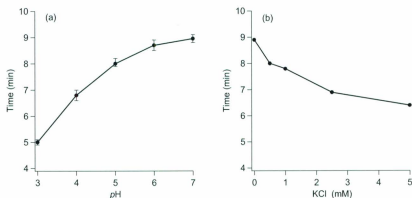


Figure 2.4: More acidic pH values (a) and lower ionic strengths (b) increase the amount of time required for membrane formation. The lines connecting the data points serve as guides to the eye and the uncertainty estimates associated with each data point in (b) are contained within the size of the markers.

2.4 Results

2.4.1 Membrane formation

The speed of membrane formation can be adjusted by changing cell geometry, applied voltage or electrolyte composition. The onset of film formation, viewed easily with the naked eye, is very reproducible for experiments using the same electrode geometry and spacing (for example, ~ 9 minutes for pH 7 electrolytes exposed to 8 V from parallel plate electrodes 2.5 cm apart). Larger voltages or closer electrode spacings lead to faster film formation because of higher current density. Electrolytes whose initial pH values are further from the isoelectric point of collagen ($pH \sim 6.5$ in these experiments^{14, 22}) require longer times to form the collagen membranes (Figure 2.4a). Finally, film formation time decreases slightly with increasing ionic strength of the electrolyte. Figure 2.4b illustrates this effect with the addition of KCl; similar trends were observed with $CaCl_2$ and $NaCl$.

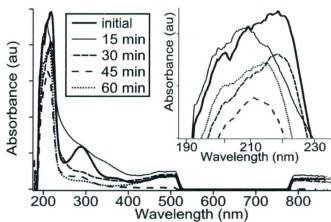


Figure 2.5: UV-Vis absorption spectra of post-deposition electrolytes show that longer exposure to the applied potential leads to a decrease in the collagen-related absorbance peak near 200 nm (inset), corresponding to more collagen incorporation into the membrane. The marker spacings on the ordinate axes are consistent for the main graph and the inset.

Although electrolyte composition differences can change how rapidly the initial membrane forms, the membrane continues to grow over time as long as the applied cell voltage remains. Figure 2.5 shows absorbance *vs.* wavelength data from the post-synthesis electrolytes (initial *pH* 7) after exposure to the applied potential for different amounts of time. All initial and final electrolytes were colorless, so no peaks were obtained in the visible region. However, the intensities of the broad peaks near 200 nm (originating from peptide bonds) and 300 nm (due to aromatic amino acid side chains, prominent only in the initial electrolyte prior to aggregation) decrease with increasing electrosynthesis time, suggesting that collagen is continually removed from the electrolyte as it is incorporated into the membrane. We note that there was little difference in absorbance spectra as a function of electrolyte *pH* or ion concentration for the same times and applied potentials. Membrane thickness also increases with electrosynthesis time, consistent with the optical absorption data trends in Figure 2.5. AFM data indicate thicknesses ranging from 240 ± 20 nm at 15 minutes to 420 ± 50 nm at 60 minutes. We conclude that increasing the time allowed for electrosynthesis is more effective at growing the membrane than merely changing the ionic content of the electrolyte. All subsequent data presented here will correspond to films electrosynthesized for 30 minutes, unless otherwise indicated.

2.4.2 Correlating mechanical stiffness with fibril content

We quantified Young's moduli for electrosynthesized collagen membranes based on data from AFM indentation curves on dried membranes. The models we propose for membrane formation and stiffness control arise from assessments of relative changes in the Young's moduli, rather than on their absolute values, but it is reassuring that the values for our dried membranes do lie within the broad range (0.2–3 GPa) of Young's moduli that have been reported for collagen fibrils.^{23–25}

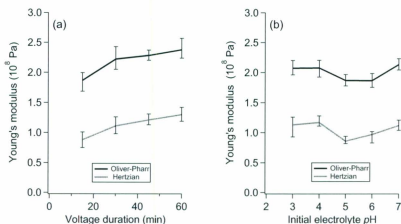


Figure 2.6: Young's modulus values for electrosynthesized collagen membranes change as two parameters were varied independently: (a) duration of applied voltage (at pH 7) and (b) initial electrolyte pH value (for 30 minute voltage duration). Error bars correspond to a set of measurements made with the same tip on the same sample. Trends are qualitatively similar using either Hertzian or Oliver-Pharr models for tip-sample contacts.

Figure 2.6 shows representative data that confirm that electrosynthesis conditions can influence membrane stiffness. These data also indicate that there is a striking spatial uniformity in the mechanical responses of the membranes. While AFM indentation is intrinsically a local measurement, the stiffness variations across a given membrane (error bars) are smaller than the changes observed under different synthesis conditions (trend lines). To understand this, it is important to recognize that an indentation with our probe will access a depth 100-200 nm and initiate a rather large contact area (with diameter 100-200 nm) involving a network of monomers and/or fibrils. Therefore, although more mature fibrils could be broader than the tip diameter (~ 20 nm), indentation does not necessarily measure the modulus of a single fibril. Figure 2.6 also demonstrates that moduli calculated from Hertzian (Equation 2.1) and Oliver-Pharr (Equation 2.3) models showed qualitatively similar trends for all samples. This suggests that the stiffness trends we observe are not dependent on the details of how the tip-sample interactions are modeled.

The Young's modulus shows a marked increase ($\sim 40\%$) over the first 30 minutes of membrane formation (Figure 2.6a). We note that this trend cannot be attributed to substrate artifacts affecting probe indentation, since membranes are also increasing in thickness over time. Instead, we attribute this stiffness increase to higher fibril content in the membrane, confirmed with Raman scattering data (Figure 2.7a,c) based on assignments of the amide III regions (560 cm^{-1} and $1240\text{-}1270\text{ cm}^{-1}$, associated with fibrilized collagen) and the C-N stretch regions (1095 cm^{-1} and 1454 cm^{-1} , predominant for monomeric collagen).^{26, 27} The increasing background level for higher wavenumbers is generally characteristic of monomeric samples with some denaturation, and is therefore more prevalent for samples with higher monomer content. Because the Raman peaks of interest are broad (particularly for fibrils) and overlap with other peaks (particularly for monomers), fitting the peaks to calculate areas

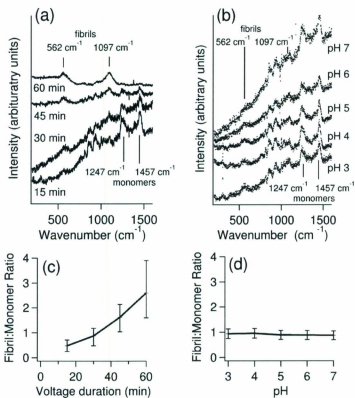


Figure 2.7: Raman spectra from collagen samples prepared with (a) different durations of applied voltage (all at pH 7) and (b) electrolytes with different initial pH values (all with 30 minutes of applied voltage). Spectra are offset along the intensity axis for clarity. Estimates of fibril to monomer ratio based on peak height comparisons from these spectra show (c) more distinctive fibril signatures for longer duration of applied voltage, and (d) a slight decrease of fibril content when the electrolyte pH is near the isoelectric point of collagen.

would introduce more parametrization than the data could justify. Peak height was therefore a more consistent and reliable means to approximate the relative changes in monomer and fibril content.

Another factor that has a more moderate effect on membrane stiffness is the initial pH of the starting electrolyte. Adjusting the initial electrolyte pH to 5–6 slightly lowers the membrane Young's modulus (Figure 2.6b). This trend is harder to correlate with the membranes' relative monomer and fibril contents, unlike the membrane stiffening observed with longer electrosynthesis times. Figure 2.7b,d shows that the initial electrolyte pH has little effect on relative monomeric and fibrillar composition of the resulting membranes.

Since the pH region that leads to less stiff membranes coincides with the isoelectric point for collagen in these experiments,^{14, 22} this softening is likely related to pre-aggregation of collagen in the electrolyte, prior to incorporation in the membrane. As illustrated schematically in Figure 2.1, the non-specific aggregates could not mature into fibrils, and thus their incorporation would likely lead to a softer membrane. Earlier studies provide further support for these conclusions, showing that the specificity of collagen aggregates can be strongly affected by pH and concentration conditions.^{8, 14, 27, 28} The error bars in Figure 2.7c,d correspond to a set of measurements made with the same sample in various locations.

T-tests were performed using *R Gu*²⁹ software to verify whether the elastic moduli of the membranes prepared using various pH electrolytes differ or lie in the same distribution. The t-test calculates the probability (P) that the mean values for two data sets would have the same values with 95% confidence. The results show that the probability for the elastic moduli to be similar for the membranes prepared with pH 3 and pH 4 electrolytes is ~ 0.2 , so the values in the two sets are overlapping. In contrast, the elastic moduli sets for the membranes prepared with pH 4 and pH

Table 2.3: T-test comparisons of the elastic moduli (Oliver-Pharr) of collagen membranes prepared using different pH electrolytes.

Set I	Set II	Elastic modulus ($\times 10^8$ Pa)		Probability (P)
		Set I	Set II	
pH 3	pH 4	2.21	2.27	0.19
pH 4	pH 5	2.27	1.90	0.0007
pH 5	pH 6	1.90	1.96	0.60
pH 6	pH 7	1.96	2.23	0.003

5 electrolytes have the probability of ~ 0.0007 thus showing that the values lie in entirely different regions. More results are given in Table 2.3.

2.4.3 Ion-dependent softening and stiffening

Addition of biologically relevant ions to the electrolyte led to a range of Young's modulus changes, as shown in Figure 2.8. Ca^{2+} ions have been reported to enhance collagen aggregation during electrochemical processes³⁰ and to accelerate both the nucleation and growth of collagen fibrils.³¹ Correspondingly, we observe larger Young's moduli (Figure 2.8a) after adding up to 10 mM CaCl_2 to the starting electrolyte. On the other hand, KCl addition leads to substantially lower Young's moduli (Figure 2.8b), even though other reports have also suggested that K^+ promotes collagen aggregation.³² The changes we observe with the addition of CaCl_2 and KCl contrast with the minimal effect that similar concentrations of NaCl have on stiffness (Figure 2.8c).

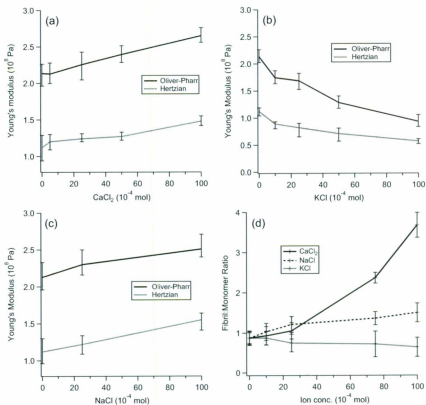


Figure 2.8: Young's moduli values can change dramatically with the addition of different concentrations of (a) CaCl₂ or (b) KCl, with smaller changes for the addition of (c) NaCl to the electrolyte. Stiffness trends follow changes in the relative amount of fibrillar collagen (d, as determined from Raman scattering peak intensities), with stiffer membranes displaying higher fibril content.

Table 2.4: T-test comparisons of the elastic moduli (Hertzian) of collagen membranes prepared with the addition of various salts.

Set I	Set II	Elastic modulus ($\times 10^8$ Pa)		Probability (P)
		Set I	Set II	
No added salt	10 mmol CaCl_2	1.11	1.48	6×10^{-6}
No added salt	10 mmol NaCl	1.11	1.35	3×10^{-3}
No added salt	10 mmol KCl	1.11	0.58	4×10^{-10}

T-tests were carried out to compare the elastic moduli of the membranes prepared with and without any added salt. Table 2.4 shows the mean elastic moduli (Hertzian model) and the probability (P) for the values to be in similar range for the addition of any salt. The lower probability values (6×10^{-6} and 3×10^{-3}) show that there are significant differences in the elastic moduli prepared with and without CaCl_2 or KCl. In contrast, the probability is higher for NaCl, thus indicating that addition of NaCl has a statistically insignificant effect on the elastic moduli of collagen membrane.

T-tests on elastic moduli obtained by Oliver-Pharr model also show the same trend. The results show that there are definite differences in the elastic moduli (Oliver-Pharr) for the membranes prepared without and with higher concentration of CaCl_2 ($P \sim 7 \times 10^{-5}$) or KCl ($P \sim 1 \times 10^{-8}$). In contrast, the elastic moduli for the membranes prepared with and without addition of higher concentration of NaCl have a slight difference with $P \sim 0.08$.

These disparate stiffness trends as a function of ion concentration track very well with changes in the relative amounts of fibrillar and monomeric collagen (Figure

2.8d) as assessed from Raman scattering spectra. The stiffest membranes, prepared in electrolytes containing 10 mM CaCl_2 , display the highest relative fibril content. In contrast, membranes prepared in electrolytes with high KCl levels were mechanically weak and easily dissociable when rinsed in water, suggesting non-specific aggregation. Correspondingly, Raman peak intensities suggest a slightly lower fibril content. NaCl-containing electrolytes yield membranes with only slightly enhanced fibril content with increasing $[\text{Na}^+]$ (Figure 2.8c).

We investigated the degree of collagen aggregation in the electrolyte after ~ 5 minutes of applied voltage, just prior to any visible membrane formation. Aliquots of the electrolyte were removed from the center of the electrochemical cell in the vicinity where the membrane would eventually form. The aliquots were then spread on a glass microscope slide and allowed to dry under ambient temperature and humidity conditions. Since the amount of collagen obtained from these aliquots is too low to obtain meaningful results from Raman measurements regarding relative monomer and fibril content, we used atomic force microscopy (AFM) images for qualitative indications of fibril formation.

Figure 2.9 shows representative AFM images of the dried electrolyte aliquots obtained immediately before visible membrane formation, contrasting the differences among electrolytes that yielded membranes with very different Young's moduli values. For example, Figure 2.9a shows that the Ca^{2+} -containing electrolyte (which produced the stiffest films with the highest relative fibril content as measured by Raman spectroscopy) reveals very little fibrillar collagen relative to the reference electrolyte (Figure 2.9b) or the K^+ -containing electrolyte (Figure 2.9c, which produced the softest films with the lowest relative fibril content). Thus, these data suggest that rapid fibril formation in the electrolyte reduces the propensity of fibril incorporation in the membrane. This observation can be explained in the context of earlier

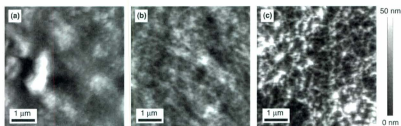


Figure 2.9: Representative AFM images of dried electrolyte aliquots obtained immediately before visible membrane formation (5 minutes of applied electric field) in electrolytes containing (a) 10 mM Ca^{2+} , (b) no Ca^{2+} or K^+ , and (c) 10 mM K^+ . Fibrillar topographic features are least prevalent in the 10 mM Ca^{2+} aliquot, even though the membranes produced from that electrolyte show the highest relative fibril content in Raman data.

studies that have shown that fibrillar collagen migrates more slowly in electric fields than monomeric collagen.²⁷ Therefore, AFM data suggest that the origin of the ion-related stiffness differences are likely related to aggregation differences that occur in the electrolyte prior to membrane formation.

AFM images also provide strong evidence that collagen fibrils will grow when they are exposed to an electric field for an extended period of time, whether in the electrolyte or part of the membrane. After 30 minutes of applied electric field to a Ca^{2+} -containing electrolyte (10 mM), we compared dried electrolyte obtained near the cathode (Figure 2.10a) and anode (Figure 2.10b, obtained *after* membrane formation) with images of the membrane itself (Figure 2.10c,d). Fibrillar collagen is more prevalent in the aliquots exposed to the electric field for longer times (30 minutes, in Figure 2.10a,b) compared to those exposed for shorter times (5 minutes, Figure 2.10a).

Within the membrane, there is also evidence that fibrils grow over time. It is important to remember that the membrane continues to grow in thickness with increasing

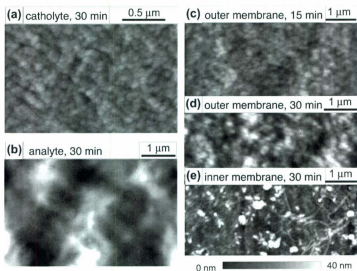


Figure 2.10: Representative AFM images show that fibrils grow when in the presence of an applied electric field, both in the electrolyte (a,b) and in the membrane itself (c,d,e). All images shown here are from experiments with electrolytes containing 10 mM Ca^{2+} . Dried electrolyte aliquots show more fibrils in both the (a) alkaline and (b) acidic electrolytes. Images of the outermost layer of the membrane formed in 15 minutes (c) or 30 minutes (d) show less fibril content. The ethanol rinsed membrane (e) shows considerably more fibrillar topographies.

duration of the applied electric field, which indicates that collagen is continually added to the membrane. Thus, the outermost parts of the membrane will contain the most recently added collagen. Based on the faster migration times of monomeric collagen relative to fibrillar collagen, as described above, it is not surprising that AFM images, providing information on the topography of the outermost layers of the membrane, show very little evidence of fibrillar collagen and very little change in topography among membranes prepared with different durations of the applied field (Figure 2.10c,d). However, when the outermost layer is stripped away (in this case, with an ethanol rinse, as shown in Figure 2.10e), the inner part of the membrane shows clear evidence of fibrillar collagen. Since the electrolyte had relatively little fibril content immediately prior to membrane formation (Figure 2.10a), these data suggest that fibrils must grow and mature within the membrane much as they do in the electrolyte (Figure 2.10a,b) when exposed to an applied electric field.

2.5 Discussion and conclusions

This work demonstrates that mechanical stiffness is a useful metric for characterizing complex collagen assemblies, providing insight about the relative importance of non-specific *versus* hierarchical aggregation products and pathways in collagen-based materials. The trends in the stiffness data are consistent whether the tip-membrane interactions are modeled with a Hertzian approach or the Oliver-Pharr model. Thus, the details of the tip-membrane interactions do not appear to affect the overall conclusions we draw from the data.

With a correlation established between the degree of fibril content and the stiffness of the electrochemically synthesized collagen membranes, we investigated the points in the synthesis process at which fibril formation could occur, and whether the coexis-

tence of fibrils and monomers contributed to lateral uniformity in membrane stiffness. Because collagen fibrillogenesis is a hierarchical process,⁵ the direct addition of monomers (from the electrolyte) cannot itself create more fibrils in the membrane (Figure 2.1). Instead, protofibrils must form at some point during the electrosynthesis process, either in the electrolyte or in the membrane itself. We see evidence of protofibrils in AFM images (Figure 2.10) of air-dried aliquots of electrolyte removed immediately prior to membrane formation, but qualitative comparisons showed that the Ca^{2+} -containing electrolyte (which produced the stiffest films with the highest relative fibril content) contained very little fibrillar collagen relative to the K^+ -containing electrolyte (which produced the softest films with the lowest relative fibril content). Since limited fibril formation in the electrolyte appears to correlate with higher fibril content in the membrane, and *vice versa*, it appears that fibrils must be able to grow within the membrane, and not just in the electrolyte.

Fibrils mature over time, so it is not surprising that longer electrosynthesis times lead to stiffer films. Similarly, it is reasonable to expect that initial electrolyte pH values close to the monomeric isoelectric point are more likely to promote non-specific aggregation at the expense of fibril formation, thereby leading to softer membranes. It is more complicated to explain the stiffness differences that arise from membranes prepared in the presence of different cations. K^+ and Ca^{2+} ions were selected because they have both been shown to promote collagen fibrillogenesis.³⁰⁻³² However, the cation effects on membrane stiffness are dramatically different, with increased K^+ concentrations leading to collagen aggregation in solution, at the expense of fibril growth within the membrane. In contrast, Ca^{2+} promotes fibril maturation within the membrane, leading to higher fibril (rather than protofibril or monomer) content within the membrane and hence a higher Young's modulus. The precise role of these cations in the hierarchical assembly of collagen fibrils is not understood, although it has

been suggested that the ions promote lateral aggregation of monomers or protofibrils through a range of mechanisms, including bridging or affecting the isoelectric point of the protein through binding to amino acid side chains.³⁰⁻³² In the particular case of our reaction conditions, it appears that Ca^{2+} is required for higher-order fibril growth, perhaps due to its higher charge density (divalent and smallest of the three cations selected) allowing for better protofibril bridging.

References

- [1] Silver, F.; Christiansen, D.; Snowhil, P.; Chen, Y. *Connective Tissue Research* **2000**, *41*, 155-164.
- [2] Silver, F. H.; Freeman, J. W.; Seehra, G. P. *J. Biomech.* **2003**, *36*, 1529-1553.
- [3] Cheng, X.; Gurkan, U. A.; Dehen, C. J.; Tate, M. P.; Hillhouse, H. W.; Simpson, G. J.; Akkus, O. *Biomaterials* **2008**, *29*, 3278-3288.
- [4] Guo, S. L.; Akhremitchev, B. B. *Biomacromolecules* **2006**, *7*, 1630.
- [5] Kadler, K.; Holmes, D.; Trotter, J.; Chapman, J. *Biochem J* **1996**, *316*(Pt 1), 1-11.
- [6] MacNeil, S. *Nature* **2007**, *445*, 874-880.
- [7] Zani, B. G.; Kojima, K.; Vacanti, C. A.; Edelman, E. R. *Proc. Nat. Acad. Sci.* **2008**, *105*, 7046-7051.
- [8] Köster, S.; Leach, J. B.; Struth, B.; Pfohl, T.; Wong, J. Y. *Langmuir* **2007**, *23*, 357-359.
- [9] Guo, C.; Kaufman, L. *Biomaterials* **2007**, *28*, 1105-1114.

- [10] Evans, H. J.; Sweet, J. K.; Price, R. L.; Yost, M.; Goodwin, R. L. *Am. J. Physiol. Heart Circ. Physiol.* **2003**, *285*, H570-578.
- [11] Lee, P.; Lin, R.; Moon, J.; Lee, L. P. *Biomed. Microdev.* **2006**, *8*, 35-41.
- [12] Denis, F. A.; Pallandre, A.; Nysten, B.; Jonas, A. M.; Dupont-Gillain, C. C. *Small* **2005**, *1*, 984-991.
- [13] Marino, A. A.; Becker, R. O. *Calc. Tiss. Res.* **1970**, *4*, 330-338.
- [14] Baker, H. R.; Merschrod S., E. F.; Poduska, K. M. *Langmuir* **2008**, *24*, 2970-2972.
- [15] Matthews, J. A.; Wnek, G. E.; David G. Simpson, D. G.; Bowlin, G. L. *Biomacromolecules* **2002**, *3*, 232-238.
- [16] Hutter, J. L.; Bechhoefer, J. *Rev. Sci. Instrum.* **1993**, *64*, 1868-1873.
- [17] Akhremitchev, B. B.; Walker, G. C. *Langmuir* **1999**, *15*, 5630-5634.
- [18] Hay, J. L.; Wolff, P. J. *J. Mater. Res* **2001**, *16*, 1280-1286.
- [19] Pharr, G.; Oliver, G.; Brotzen, F. *J. Mater. Res* **1992**, *7*, 613.
- [20] Oliver, W.; Pharr, G. *J. Mater. Res* **2004**, *19*, 3.
- [21] Pharr, G. M.; Bolshakov, A. *J. Mater. Res.* **2002**, *17*, 2660-2671.
- [22] Taylor, S. *Advances in Food and Nutrition Research*; Academic Press, Burlington, MA 01803, USA: 2010.
- [23] Sasaki, N.; Odajima, S. *J. Biomechanics* **1996**, *29*, 655-658.
- [24] van der Rijt, J. A. J.; van der Werf, K. O.; Bennink, M. L.; Dijkstra, J. P.; Feijen, J. *J. Macromol. Biosci.* **2006**, *6*, 697-702.

- [25] Heim, A. J.; Matthews, G. W. *Appl. Phys. Lett.* **2006**, *89*, 181902.
- [26] Wisniewski, M.; Sionkowska, A.; Kaczmarek, H.; Lazare, S.; Tokarev, V.; Belin, C. *J. Photochem. Photobio. A: Chem.* **2007**, *188*, 192-199.
- [27] Huelin, S. D.; Baker, H. R.; Poduska, K. M.; Merschrod S., E. F. *Macromolecules* **2007**, *40*, 8440-8444.
- [28] Gobeaux, F.; Mosser, G.; Anglo, A.; Panine, P.; Davidson, P.; Giraud-Guille, M.-M.; Belamie, E. *J. Mol. Biol.* **2008**, *376*, 1509-1522.
- [29] "R Gui is available for free at <http://cran.r-project.org/bin/windows/base/>", Last accessed on November 2011.
- [30] Fan, Y.; Duan, K.; Wang, R. *Biomaterials* **2005**, *26*, 1623-1632.
- [31] Evans, C. H.; Drouven, B. J. *Biochem. J.* **1983**, *213*, 751-758.
- [32] Freudenberg, U.; Behrens, S. H.; Welzel, P. B.; Müller, M.; Grimmer, M.; Salchert, K.; Taeger, T.; Schmidt, K.; Pompe, W.; Werner, C. *Biophys. J.* **2007**, *92*, 2108-2119.

Chapter 3

Collagen-membrane-induced calcium phosphate electrocrystallization *

3.1 Introduction

There is an urgent demand for bone healing materials because conventional bone replacement metals and alloys, while mechanically strong, do not usually stimulate cell growth.^{1, 2} Bone is a complex composite comprised of mineral and proteinaceous components. Although collagen is the main matrix constituent in bone, there is evidence that non-collagenous proteins also contribute to calcium phosphate mineralization.^{3, 4} Rather than attempting to mimic the complex *in vivo* bone regeneration process, there has been considerable scientific effort devoted to the development of *in vitro* methods

*This chapter was published as "Collagen-membrane-induced calcium phosphate electrocrystallization" M. Ramesh Kumar, Erika F. Merschrod S., Kristin M. Poduska, *Crystal Growth & Design* **2011**, *11* 26–28. Used with permission.

The candidate contributed to experimental design, collected and analyzed all data, wrote the initial draft of the manuscript, and contributed to manuscript revisions.

to produce collagen-calcium phosphate composites that can be used to enhance bone healing.^{5,6} Challenges in the production of such composites include phase selectivity of the mineral component (to control reactivity and solubility) and adhesion between the protein and mineral component (for enhanced mechanical stability).

This work describes an electrochemical isoelectric focusing method that yields collagen-calcium phosphate composites with controlled phase and excellent adhesion between mineral and collagen. Previous work^{7,8} describes the electrochemical aggregation of pure collagen into a membrane *via* isoelectric focusing. Here, we demonstrate that this electrochemically aggregated collagen can act as a scaffold for calcium phosphate mineralization, and that it also affects the nucleation and growth process of the mineral. This method offers a distinct advantage over many other electrochemical techniques⁹⁻¹³ used to produce calcium phosphate-collagen coatings because it offers the flexibility of producing a scaffolded composite without need of a supporting substrate.

3.2 Experimental procedure

Composites were made by a simple two-step process, shown schematically in Figure 3.1. First, collagen membranes were prepared from electrolyte containing type I collagen monomers (final concentration of 0.15 mg/mL from 6.4 mg/mL acidic Nutragen stock solution (Inamed Biomaterials)) in ultrapure water (Barnstead, 18.2 M Ω -cm) with NaOH (EMD Chemicals, ACS reagent grade) to adjust the electrolyte pH to 7. When the amphoteric collagen monomer is exposed to the pH gradient produced by water electrolysis at the electrodes (8 V between two stainless steel parallel plate electrodes), a collagen film forms parallel to and approximately mid-way between the electrodes, where the pH matches the isoelectric point of collagen. After suffi-

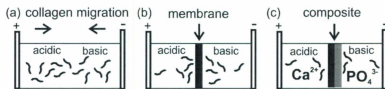


Figure 3.1: A schematic illustration of the two-step process for preparing the membrane-based electrosynthesized collagen-mineral composite. An applied voltage is required both to form the collagen membrane (Step 1) and to stimulate crystallization of the calcium phosphate on the membrane (Step 2). The acidic and basic regions are produced by water electrolysis and are maintained after the membrane forms.

cient collagen film accumulation (30 minutes), or after the insertion of a cellulose membrane (Spectra/Por Biotech RC Membrane, MWCO: 8000, Spectrum Laboratories Inc.), calcium (either CaCl_2 or $\text{Ca}(\text{NO}_3)_2$, Aldrich Chemicals, ACS reagent grade) and phosphate (K_2HPO_4 or NaH_2PO_4 or $\text{NH}_4\text{H}_2\text{PO}_4$, Aldrich Chemicals, ACS reagent grade) salts were added to the acidic and basic sides, respectively, inducing calcium phosphate formation on the alkaline side of the membrane. Salt concentrations of less than 0.025 M led to an immeasurably low quantity of calcium phosphate on the membrane; higher concentrations (investigated up to 0.1 M) did not generally impact mineral phase selectivity. For subsequent analyses, the membrane-based composite was air dried on a glass slide.

For comparison, electrochemical precipitation experiments followed the same procedure as with the membrane, but using an electrolyte without collagen. In addition, simple solution mixing methods were investigated, wherein calcium and phosphate salt solutions (0.1 M, 1000 μL each) were combined to form calcium phosphate precipitates that were subsequently rinsed with ultrapure water and air-dried.

3.3 Results and discussion

Mineral phases were identified with infrared spectroscopy (FTIR, Bruker Alpha, transmission mode with KBr matrix, 0.9 cm^{-1} resolution). Each spectrum was collected from an entire composite membrane, prepared under comparable conditions, so it is reasonable to make qualitative comparisons of relative peak heights between protein and mineral components among different specimens. Energy dispersive X-ray (EDX, Rontec Quantax with software from JKTech, University of Queensland, Australia) data further confirmed the phase assignments. Phase identification from X-ray diffraction data was not conclusive due to small sample volumes. In general, amorphous materials (such as ACP) and poorly crystalline materials (such as CHAP) cannot be readily differentiated *via* XRD because of their non-existent or broad diffraction peaks, respectively.¹³ Microstructural information came from scanning electron microscopy (SEM, FEI Quanta 400 environmental) on samples dried onto metal pucks and then carbon-coated. Elastic modulus values were obtained using an atomic force microscope (Asylum Research MFP-3D) using a method described elsewhere⁸ (Chapter 2).

3.3.1 Electrolyte composition and concentration effects

The results show that the presence of the collagen membrane, in addition to the use of electrochemically controlled precipitation, impacts mineral phase selectivity. For example, infrared (IR) spectra indicate brushite ($\text{CaHPO}_4 \cdot 2\text{H}_2\text{O}$) formation from a simple mixing of a phosphate solution ($0.1\text{ M K}_2\text{HPO}_4$) with either 0.1 M CaCl_2 or CaNO_3 , while electrochemical methods applied to the same starting solutions yield amorphous calcium phosphate (ACP). Comparisons between collagen-membrane-based, electrochemical, and solution production using a variety of starting

Table 3.1: Comparison of mineral products resulting from an electrochemically (EC) produced collagen membrane composite, electrochemically assisted precipitation or solution precipitation using different starting electrolytes. Control experiments performed with a cellulose membrane did not yield a measurable amount of mineral on the membrane.

Ca ²⁺ source	PO ₄ ³⁻ source	collagen membrane EC product	EC product	solution product
CaCl ₂	K ₂ HPO ₄	CHAp	ACP	brushite
CaCl ₂	KH ₂ PO ₄	CHAp	ACP	brushite
CaCl ₂	NaH ₂ PO ₄	CHAp	CHAp	none
CaCl ₂	NH ₄ H ₂ PO ₄	brushite	ACP	none
Ca(NO ₃) ₂	K ₂ HPO ₄	CHAp	CHAp	brushite
Ca(NO ₃) ₂	KH ₂ PO ₄	CHAp	CHAp	brushite
Ca(NO ₃) ₂	NaH ₂ PO ₄	CHAp	ACP	none
Ca(NO ₃) ₂	NH ₄ H ₂ PO ₄	CHAp	ACP	none

salts are summarized in Table 3.1. Carbonated hydroxyapatite (Ca₅(PO₄)₃(OH) with carbonate ions substituting for either phosphate or hydroxide,⁶ CHAp) dominates in all protein-mineral composite membranes, with one exception.

3.4 Phase selectivity

As shown in Table 3.1 and in earlier work,^{13, 14} different mineral phases can be obtained from electrochemically assisted deposition by selecting appropriate precursor

salts. In addition to the effects from using either monobasic or dibasic phosphate salts, counterions can also play a significant role, most likely from their effects on buffering (the addition of ammonium counterions) or their electrochemical activity (either nitrate or chloride counterions). For example, chloride incorporation has been observed by others,¹⁴ and it has also been reported that nitrate reduction can contribute to enhanced electrolyte alkalinity.¹³ In our studies, we find that there is surprisingly little difference in the phase selectivity when using either chloride- or nitrate-based electrolytes.

Others have shown that the formation of ACP, a precursor to the bone-like apatitic phase, requires a rapid reaction between calcium and phosphate ions, and stabilizing agents (such as Mg^{2+} or HCO_3^-) are needed to maintain ACP under ambient conditions.¹⁵ We find that select precursors yield stable amorphous calcium phosphate from electrochemically assisted syntheses, but only in the absence of collagen.

3.4.1 Collagen membrane's role in mineral growth

Figure 3.2 shows representative IR spectra that demonstrate collagen's influence on phase selectivity. Absorption peaks with wavenumbers above 1300 cm^{-1} are due to collagen, while the phosphate peaks below 1300 cm^{-1} can be assigned to the mineral component.^{11, 16} When there is no collagen present in the electrolyte, amorphous calcium phosphate (ACP) forms (PO_4^{3-} peak at 1051 cm^{-1}), but when collagen is present this peak shifts to 1035 cm^{-1} which is characteristic of CHAp's ν_3 (PO_4^{3-}) mode.¹⁷ In these and all other samples, IR spectra show a peak near 870 cm^{-1} that is indicative of carbonate incorporation. This is attributed to dissolution of ambient $\text{CO}_2(\text{g})$.^{12, 14}

The relative intensities of the phosphate absorption peaks in specimens prepared with collagen are consistently higher than those prepared without collagen. Since this

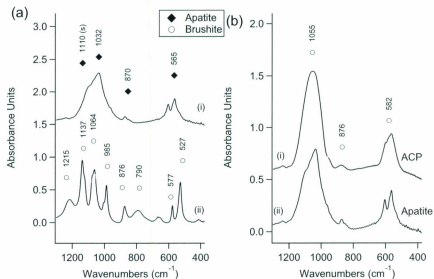


Figure 3.2: (a) Representative IR spectra for collagen-calcium phosphate composites prepared with collagen monomers plus 0.1 M CaCl_2 and either 0.1 M (i) K_2HPO_4 or (ii) $\text{NH}_4\text{H}_2\text{PO}_4$ show that precursor salts affect phase selectivity. The dominant peaks in spectrum (i) are from carbonated hydroxyapatite (CHAp) while those in (ii) indicate brushite. (b) Representative IR Spectra for specimens prepared using CaCl_2 and K_2HPO_4 , either without (i) or with (ii) collagen, highlight the importance of the presence of collagen for phase selectivity. CHAp forms in the presence of collagen; otherwise, amorphous calcium phosphate (ACP) dominates. In both panels, spectra are offset along the absorbance axis for clarity.

trend holds for comparisons among dozens of samples, it suggests that collagen also triggers increased calcium phosphate formation. This could be due to either enhanced precipitation (the membrane provides favorable nucleation sites) or trapping of the calcium phosphate particles as the collagen continues to aggregate. Scanning electron microscopy (SEM) images show evidence for crystallites forming on and within the membrane (Figure 3.3), and corresponding energy-dispersive X-ray analyses confirm that the crystallites contain calcium and phosphorous.

There are also spatial differences that occur in the presence of collagen. When no collagen is present in the electrolyte, calcium phosphate precipitates form only in very alkaline environments ($pH \geq 8$, near and on the cathode). In contrast, the presence of collagen allows crystals to grow also at the more acidic pH values present in the electrolyte near the membrane (~ 6.5). The alkaline side of the collagen membrane appears to act as a nucleation site, and the majority of the mineralization occurs directly at the collagen membrane rather than as precipitation in the electrolyte. There is no evidence of mineral formation on the glass surfaces of the electrochemical cell, but a thin calcium phosphate film does form on the stainless steel cathode, similar to earlier studies.¹³ Given the complexity of the calcium phosphate formation environment (including pH gradients and counterions), we find it quite surprising that there is no evidence of mixed phases, and that the mineralization occurred only on the alkaline side of the membrane. It is not surprising that the calcium phosphate minerals form only on the alkaline side because they dissolve in acidic solutions. The composite membranes are mechanically robust when dried, and the mineral coating is intimately incorporated into the collagen scaffold. Figure 3.4 shows that composite membranes are stiffer (higher elastic modulus values) than for non-mineralized membranes⁸ (Chapter 2). Rinsing in water or ethanol does not degrade the composites in any way.

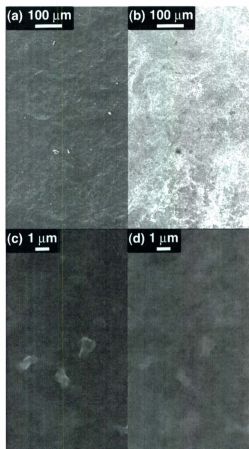


Figure 3.3: Representative SEM micrographs, at low (a, b) and high (c, d) magnifications, of a carbonated hydroxyapatite-collagen composite (here, from $\text{Ca}(\text{NO}_3)_2$ and $\text{NH}_4\text{H}_2\text{PO}_4$ precursors). The secondary electron images (a, c) show that composite topography is dominated by micron and sub-micron crystallites that appear to be embedded in the protein scaffold. The companion backscattered electron images of the identical areas (b, d) confirm that the mineral, indicated by bright regions, is spread rather uniformly throughout the scaffold.

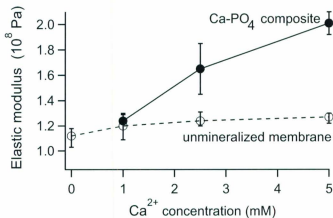


Figure 3.4: Comparison of elastic modulus values for composite mineralized collagen membranes (solid line) and unmineralized collagen membranes (dashed line). Preparing an unmineralized membrane in the presence of higher amounts of Ca^{2+} will lead to a slightly stiffer scaffold, but composite membranes are consistently more stiff. The lines connecting data points serve merely to guide the eye.

3.4.2 Collagen membrane's role in mineral nucleation

To confirm that the presence of collagen is important – and not merely the membrane-based pH partitioning that occurs during membrane formation – we replicated our experiments with a commercially available cellulose membrane. Although a small amount of calcium phosphate adhered to the cellulose, most formed as precipitates in the alkaline region of the electrolyte, similar to the case with no membrane present. In contrast, virtually no precipitates form elsewhere in the cell when collagenous membranes are present. We note that other membranes have been shown to support calcium phosphate crystallization, including a recent report of the mineralization of a polymeric membrane in the presence of an alternating (AC) electric current.¹⁸ The issues of specific chemical functionalities and local pH values undoubtedly play an important role in the calcium phosphate crystallization process in these composite

membranes. These experiments do not substantiate a probable mechanism, but recent theoretical and experimental investigations have begun to address aspects of this question.^{6, 12, 14, 15, 19}

3.5 Conclusions

In conclusion, electrochemically assisted synthesis, based on isoelectric focusing, offers an expedient way to make robust collagen-calcium phosphate composites with controlled mineral phase. Collagen not only provides a scaffold on which the mineral phase can nucleate, but its presence also triggers a strong preference for one specific mineral phase (carbonated hydroxyapatite) relative to other phases (such as brushite) that would otherwise form during electrochemical synthesis. This offers two distinct advantages for the electrosynthesized composite over many other existing biocomposite materials. First, the composite is produced as a suspended membrane that can be removed and applied to other surfaces. Second, the selectivity of the carbonated hydroxyapatite phase is fortuitous, since this is the mineral phase that is most similar to that found in natural bone. These two features make this protein-mineral composite material promising for future biocompatibility studies.

References

- [1] Stevens, M. M.; George, J. H. *Science* **2005**, *310*, 1135–1138.
- [2] Williams, D. F. *Biomaterials* **2008**, *29*, 2941–2953.
- [3] George, A.; Veis, A. *Chem. Rev.* **2008**, *108*, 4670–4693.
- [4] Meldrum, F. C.; Cölfen, H. *Chem. Rev.* **2008**, *108*, 4332–4432.

- [5] Estroff, L. A.; Hamilton, A. D. *Chem. Mater.* **2001**, *13*, 3227–3235.
- [6] Palmer, L. C.; Newcomb, C. J.; Kaltz, S. R.; Spoerke, E. D.; Stupp, S. I. *Chem. Rev.* **2008**, *108*, 4754–4783.
- [7] Baker, H. R.; Merschrod S., E. F.; Poduska, K. M. *Langmuir* **2008**, *24*, 2970–2972.
- [8] Kumar M, R.; Merschrod S., E. F.; Poduska, K. M. *Biomacromolecules* **2009**, *10*, 1970–1975.
- [9] Zhitomirsky, I. *Adv. Colloid. Interface. Sci.* **2002**, *97*, 279–317.
- [10] Cheng, X.; Filiaggi, M.; Roscoe, S. G. *Biomaterials* **2004**, *25*, 5395–5403.
- [11] Fan, Y.; Duan, K.; Wang, R. *Biomaterials* **2005**, *26*, 1623–1632.
- [12] Lu, X.; Zhao, Z.; Leng, Y. *J. Crystal Growth* **2005**, *284*, 506–516.
- [13] Huelin, S. D.; Baker, H. R.; Merschrod S., E. F.; Poduska, K. M. *Crystal Growth & Design* **2006**, *6*, 2634–2636.
- [14] Eliaz, N.; Sridhar, T. M. *Cryst. Growth. Des.* **2008**, *8*, 3965–3977.
- [15] Wang, L.; Nancollas, G. H. *Chem. Rev.* **2008**, *108*, 4628–4669.
- [16] Wisniewski, M.; Sionkowska, A.; Kaczmarek, H.; Lazare, S.; Tokarev, V.; Belin, C. *J. Photochem. Photobio. A: Chem.* **2007**, *188*, 192–199.
- [17] Rossler, S.; Sewing, A.; Stolzel, M.; Born, R.; Scharnweber, D.; Dard, M.; Worch, H. *J Biomed Mater Res A* **2003**, *64*, 655–663.
- [18] Watanabe, J.; Akashi, M. *J. Cryst. Growth* **2009**, *311*, 4323–4328.
- [19] Almora-Barrios, N.; de Leeuw, N. H. *Langmuir* **2010**, *26*, 14535–14542.

Chapter 4

Towards an artificial cornea: Electrochemical engineering of a collagen scaffold *

This work to develop an artificial cornea is done in collaboration with Drs. Robert Gendron and H el ene Paradis at the School of Medicine, Memorial University of Newfoundland. We prepare the collagen scaffolds by an isoelectric focusing method, and characterize them to determine their denaturation temperature, optical transparency and morphology by using a differential scanning calorimeter, UV-vis spectrometer and scanning electron microscope respectively. The cell viability tests to assess whether the collagen scaffolds could induce cell growth were done by Drs. Gendron and Paradis's research groups at Memorial's School of Medicine.

*Some of these data are published in "Controlled cell proliferation on an electrochemically engineered collagen scaffold" Robert Gendron, M. Ramesh Kumar, H el ene Paradis, Darryl Martin, Nhu Ho, Danielle Gardiner, Erika F. Merschrod S., Kristin M. Poduska, *Macromol. Biosci.* **2011**, In Press (DOI : 10.1002/mabi.201100341).

Except for the cell culture studies, the candidate designed and executed the experiments, analyzed the resulting data, and wrote this thesis chapter.

4.1 Introduction

In recent years, research to develop an artificial cornea has received much attention since the cornea acts as a transparent window to the eye, and any disease or damage to it directly affects the function of the eye or leads to vision loss. Millions of people affected by corneal diseases are waiting for corneal transplant surgery, and it is not always possible to replace the cornea in every case.¹ Therefore, it is necessary to develop artificial corneas, and we are very interested in this work because the main component of the cornea – the stroma – is made up of collagen.²⁻⁴

The cornea is highly transparent because its cells and proteins are highly organized to permit light to pass through them without much hindrance.⁵ In addition, there are no blood vessels present in the cornea since their presence can affect its refracting power. The thickness and diameter of the cornea are 0.5 mm and 11.5 mm respectively, and the refractive index of the cornea is almost the same as the refractive index of water.⁶ Its tissue is made up of three different layers in which the central corneal stroma is located in between the epithelium and endothelium membrane layers.⁷ More than 90% of the cornea is occupied by the stroma layer,³ and the stroma consists of collagen and water.^{5, 8}

A collagen membrane prepared by our electrochemical method can be potentially used as a matrix to synthesize an artificial cornea. There are a few main requirements for the collagen scaffold to be used as a matrix in an artificial cornea application.⁹

1. The matrix should be mechanically strong enough to withstand the pressure exerted by the eye. The average intraocular fluid pressure¹⁰ in the eye is 2.0×10^{-3} MPa.
2. The matrix needs to be extremely transparent in the visible range to maintain the high optical clarity of the eye, and it needs to be thermally stable to maintain

the protein structure.

3. The matrix has to maintain the cells in quiescent state, which means that the matrix allows the cells to grow further, but without any DNA replication.

The main goal of this work is to determine the transparency, morphology and thermal stability of the collagen membrane, and to find out how cells behave when seeded on it. In a given matrix, different kinds of cells can behave in a different way, so it is necessary to choose the appropriate cell type depending on the requirement. For our studies, we use MK/T-1 cells, which are derived from mouse corneal stromas by Gendron *et al.*¹¹

4.2 Experimental

4.2.1 Preparation of matrix scaffolds

Matrices are produced using an electrochemically induced collagen aggregation procedure that is based on isoelectric focusing between parallel plate electrodes^{12, 13} (Chapter 2). This method can be used to produce scaffolds with a wide range of dimensions ranging from sub-millimeter aggregates to scaffolds with dimensions on the order of centimeters. It is the larger scaffolds that are employed for the present study.

These membranes can be removed and air-dried on any desired substrate. Atomic force microscopy images and Raman spectroscopic data indicate that the membrane matrix has an inner core of fibrillar collagen with non-specifically aggregated monomeric collagen outer layers.¹² More details are provided in Chapter 2, Section 2.5. Membranes are removed from the electrochemical cell, placed immediately on sterile culture dishes, and refrigerated until cell culture studies commenced (Figure 4.1).

4.2.2 Characterization techniques

4.2.2.1 Differential scanning calorimetry (DSC)

To find the denaturation temperature of an electrochemically aggregated collagen membrane, a differential scanning calorimeter (Mettler Toledo STAR®) is used. For our experiments, we use a 2 °C/min scan rate, and the temperature range for the scans is 20–70 °C. Several trials were performed on different membranes prepared under the same conditions to verify the reproducibility of the data. All of our DSC experiments were performed in an N₂ environment.

4.2.2.2 UV-vis spectroscopy

We use an OceanOptics USB2000 spectrophotometer to obtain transmittance spectra from hydrated collagen membranes. For UV-vis experiments, we put the membrane on a 20 mm x 8 mm piece of a glass slide, which fits inside an UV-vis cuvette that is filled with ultrapure water (Barnstead, 18.2 MΩ-cm). We make sure that the sample in the cuvette lies in the path of UV-vis light throughout the measurement. The same sized piece of glass slide, with no collagen membrane, in a water filled cuvette is used as reference for the measurements.

4.2.2.3 Scanning electron microscopy (SEM)

A FEI Quanta 400 environmental Scanning Electron Microscope (SEM) is used in two different magnifications (1000x and 10000x) for mapping the surface morphology of the electrochemically aggregated collagen membranes.

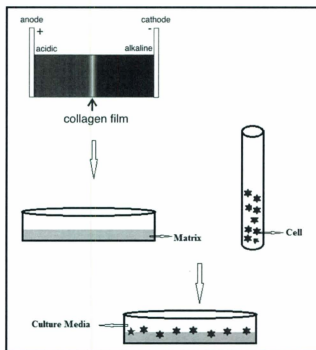


Figure 4.1: Schematic diagram for cell culture procedure. First, the collagen matrix scaffolds are prepared by an isoelectric focusing method. After synthesis, the membranes are removed using tweezers and stored in a cell culture petri dish at 4 °C. The membranes are sterilized by UV radiation to remove any biological contamination. The cell culture medium is prepared by using 10% fetal bovine serum (FBS), and the cells are grown in the culture medium with and without the collagen matrix. Cell culture is performed by placing the cell culture dishes in a tissue cell culture incubator for 48 hours in a humid, 5% CO₂ atmosphere at 37.0 °C.

4.2.2.4 Cell culture studies

The polystyrene cell culture dishes that contain the electrochemically aggregated collagen membranes are placed under UV-light (30 W / 3 A) for 10 minutes to remove any bacterial contamination present. Afterward, the cells in which we are interested are allowed to grow over the collagen membrane with 10% fetal bovine serum (FBS) culture media.^{9, 11} To gauge the cell growth over the collagen membrane, the cells are also allowed to grow in 10% fetal bovine serum (FBS) culture media without the collagen matrix.

Subsequently, the culture dishes are incubated for 48 hours in a humid 5% CO₂ atmosphere at 37.0 °C. After incubation, the cells with the collagen matrix are scraped out and centrifuged for 5 minutes at 5000 rpm to pellet them. The pellets are fixed in paraformaldehyde for 48 hours and then embedded in low melting agarose. These mixtures are embedded in paraffin blocks and then cut into 5 μm pellet sections for assessments of cell growth and controlled cell proliferation.¹¹ Hematoxylin and Eosin (H&E) staining is carried out for a few sections to enhance the phase contrast in optical microscopy.

4.3 Results and discussion

4.3.1 Thermal stability of collagen membrane

Figure 4.2 shows the DSC thermogram of an electrochemically synthesized collagen membrane. From the DSC curve, the thermal denaturation temperature of an electrochemically synthesized collagen membrane is measured as 48.6 °C. Since the denaturation temperature is much higher than the human body temperature (37.0 °C), the electrochemically aggregated collagen membranes could survive *in vivo* easily if they

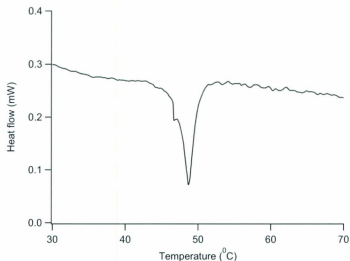


Figure 4.2: DSC thermogram of a hydrated electrochemically prepared collagen membrane shows a broad and complex protein denaturation peak at 48.6 °C.

are used as a matrix for an artificial cornea. Moreover, the denaturation temperature of our collagen is much higher than that of monomeric collagen (36.0 °C)¹⁴ and the collagen membranes prepared by other methods (37.0 °C).^{15, 16}

During heating, denaturation of collagen occurs when the triple helix disintegrates into random coils. This disintegration happens because of the rupture of *H*-bonds between the collagen polypeptide strands from the applied heat.¹⁶ The denaturation temperature (T_m) is defined as a transition midpoint, where half of the protein molecules are folded and the remaining are unfolded.

The midpoint of the transition peak gives the denaturation temperature value for the protein sample, and the sharpness of the peak can give more details about the nature of the unfolding process. If the protein is a single domain, it often gives a symmetric, narrow and single peak, and the transition between the two states is reversible. If the protein is multi-domain and has a very complex structure, the thermogram might have

several peaks from different protein domains thus making it very hard to interpret.¹⁷ Figure 4.2 shows that the thermogram for the denaturation of collagen membrane has a broad asymmetric peak at 48.6 °C. This is because the collagen might be in many different states. Some is probably monomeric and some is in fibrils of varying maturity and varying inter-connectedness. The broad peak is attributed to the broad population of structure.

4.3.2 Optical transparency of collagen membrane

Figure 4.3 shows the UV-vis spectrum of a hydrated electrochemically aggregated collagen membrane. It shows that the optical transparency of a wet membrane is very high (above 90% from 388 nm and above) in the entire visible region. Because of their high transparency, the electrochemically aggregated collagen membranes are very suitable materials for artificial cornea applications.

4.3.3 Morphology of collagen membrane

Figure 4.4 shows scanning electron microscope (SEM) images of an electrochemically assembled collagen membrane. SEM images at lower and higher magnifications (1000x and 10000x), of dried electrochemically prepared collagen matrix scaffolds show that the collagen membranes are thin sheets that can fold and form multiple layers.

4.3.4 Cell viability

Panels (a) and (b) in Figure 4.5 show phase-contrast optical microscopy images of the MK/T-1 cells cultured on the culture media with and without the collagen matrix. Figure 4.5a shows that the cell nuclei (indicated by arrows) spread broadly, which indicates that the cells grow very well and look healthy when they are cultured over

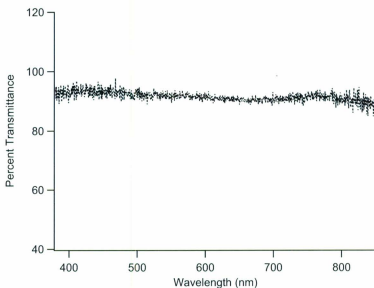


Figure 4.3: UV-vis transmittance spectrum of a hydrated collagen membrane shows the wet membrane is highly transparent and transmits more than 90% of light through it in the visible region (380–750 nm).

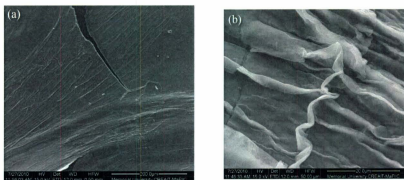


Figure 4.4: Representative scanning electron microscopy images, at two different magnifications (a) 1000x and (b) 10000x, of dried electrochemically prepared collagen matrix scaffolds highlight their sheet-like character. The scale bar in (a) is 200 μm long, and that in (b) is 20 μm long.

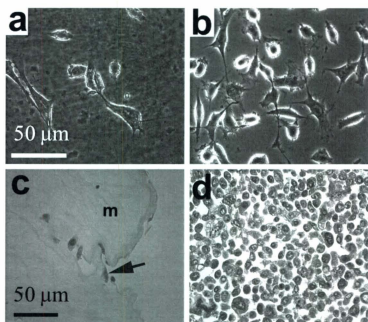


Figure 4.5: (a,b) Phase contrast optical microscopy images of MK/T-1 cells grown in 10% FBS cell culture media with and without presence of the collagen scaffold matrix show that the cells grow very well over the collagen matrix (a), similar to the cells cultured in cell culture plastic (b). Panels (a) and (b) have the same scale. (c,d) Phase contrast optical microscopy images of H&E stained sections of cultured cells; (c) in collagen matrix; (d) on plastic. The images show that the cells prefer to adhere at the edges of the collagen scaffold rather than growing over them. Panels (c) and (d) have the same scale.

collagen membrane, like the cells cultured under similar conditions without the collagen matrix (Figure 4.5b). The extensive pseudopodia (temporary projections of the cells) show that the cells are adhesive and move actively over the collagen matrix. The images of the H&E stained sections of matrix cultured (Figure 4.5c) and plastic cultured (Figure 4.5d) cells show that the cells grow on the edges of the collagen matrix (the cell nuclei are shown with arrows). From all of these images it is understandable that the cells are alive and healthy because the cell nuclei are not fragmented or wrinkled. The cells grow only at the top layer of the membrane, not in the inner layers.

4.3.5 Controlled cell proliferation

A necessary requirement for the matrix to be used in an artificial cornea is that the matrix scaffolds should maintain the cells in a quiescent state, in which the cells stay alive without replicating their DNA. To analyze this, the MK/T-1 cells are cultured along with Bromodeoxyuridine (BrdU) in the presence and absence of the collagen scaffold matrix. BrdU is only incorporated if DNA replication is occurring, and if there is no DNA replication, then there will not be BrdU staining.¹⁸

Figure 4.6 shows optical microscopy images of cells cultured with BrdU on plastic (a) and matrix (b). The cells cultured in the presence of collagen matrix show less BrdU staining than the cells cultured on plastic. This implies that the collagen matrix does not support cell DNA replication, but the plastic does.

4.4 Conclusions

The results obtained using UV-vis spectroscopy show that the electrochemically synthesized collagen membranes are highly transparent and allow more than 90% of

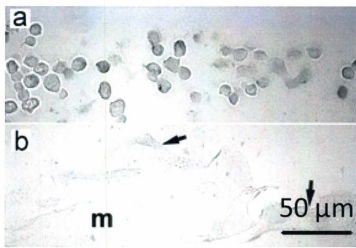


Figure 4.6: (a,b) Phase contrast optical microscopy images of MK/T-1 cells grown in presence of Bromodeoxyuridine(BrdU); (a) in plastic and (b) in collagen matrix. The BrdU staining is less pronounced in the matrix grown cells compared to the cells grown in plastic, which confirms that the collagen scaffold does not allow the cells to proliferate. Cells are indicated with arrows and 'm' denotes the matrix. Panels (a) and (b) have the same scale.

visible light to pass through them when they are hydrated. DSC thermograms indicate that the collagen membrane is highly thermostable, suggesting that it will not degrade at body temperature if used as a matrix for an artificial cornea. The MK/T-1 cells grow very well over the collagen membrane, like they do in a normal cell culture medium. The cells prefer to attach to the edges and the top layer of the collagen membrane rather than entering the inner core of the membrane. The experiments performed using Bromodeoxyuridine (BrdU) prove that the collagen membranes do not support DNA replication, which is one of the main requirements for the membrane to be used as a matrix in artificial cornea applications.

References

- [1] Liu, W.; Deng, C.; McLaughlin, C. R.; Fagerholm, P.; Lagali, N. S.; Heyne, B.; Scaiano, J. C.; Watsky, M. A.; Kato, Y.; Munger, R.; Shinozaki, N.; Li, F.; Griffith, M. *Biomaterials* **2009**, *30*, 1551–1559.
- [2] Kannabiran, C. *J. Genet.* **2009**, *88*, 487–494.
- [3] Leonard, D. W.; Mee, K. M. *Biophys. J* **1997**, *72*, 1382–1387.
- [4] Dische, Z.; Cremer-Bartels, G.; Kaye, G. I. *Proc. Natl. Acad. Sci. USA* **1985**, *82*, 760–764.
- [5] Hassell, J. R.; Birk, D. E. *Exp. Eye. Res* **91**, 2010, 326–335.
- [6] Romer, A. S.; Parsons, T. S. *The Vertebrate Body*; Holt-Saunders International, Philadelphia, PA: 1977.

- [7] Proulx, S.; Uwamaliya, J. D.; Carrier, P.; Deschambeault, A.; Audet, C.; Giasson, C.; Guérin, S. L.; Auger, F. A.; Germain, L. *Mol. Vis* **2010**, *16*, 2192-2201.
- [8] Fratzl, P.; Daxer, A. *Biophys. J.* **1993**, *64*, 1210-1214.
- [9] Gendron, R.; Kumar, M. R.; Paradis, H.; Martin, D.; Ho, N.; Gardiner, D.; Merschrod S., E. F.; Poduska, K. M. *Macromol. Biosci.* **2011**, DOI : 10.1002/mabi.201100341.
- [10] Jonas, J. B.; Degenring, Robert. Fand Kreissig, I.; Akkoyun, I.; Kampeter, B. A. *Ophthalmology* **2005**, *112*, 593-598.
- [11] Gendron, R. L.; Liu, C. Y.; Paradis, H.; Adams, L. C.; Kao, W. W. *Mol. Vis* **2001**, *7*, 107-113.
- [12] Kumar M. R.; Merschrod S., E. F.; Poduska, K. M. *Biomacromolecules* **2009**, *10*, 1970-1975.
- [13] Baker, H. R.; Merschrod S., E. F.; Poduska, K. M. *Langmuir* **2008**, *24*, 2970-2972.
- [14] Leikina, E.; Merts, M. V.; Kuznetsova, N.; S, L. *Proc. Nat. Acad. Sci. USA* **2002**, *99*, 1314-1318.
- [15] Zhang, Z.; Li, G.; Shi, B. *J. Soc. Leath. Tech. Chem* **2005**, *90*, 23-28.
- [16] Li, Y.; Li, Y.; Du, Z.; Li, G. *Thermochimica. Acta* **2008**, *469*, 71-76.
- [17] Bruylants, G.; Wouters, J.; Michaux, C. *Curr. Med. Chem.* **2005**, *12*, 2011-2020.
- [18] Taupin, P. *Brain. Res. Rev* **2007**, *53*, 198-214.

Chapter 5

Analyzing the internal pore structure of collagen membranes using single particle tracking (SPT)

5.1 Introduction

Single particle tracking (SPT) is an easy and highly reliable method to probe the internal structure of collagen membranes. Scanning Electron Microscopy (SEM) and Transmission Electron Microscopy (TEM) are used widely to investigate the mesoporous structures of polymers and membranes.¹ However, electron microscopy needs a dry sample with a conductive surface coating, and sometimes requires staining to enhance contrast in samples with small atoms (as in protein samples such as ours). On the other hand, SPT allows the sample to be in a biochemical environment, which allows us to probe the sample in a state more similar to how it would exist *in vivo* (such as in an implant).²

SPT can be effectively used to investigate the internal structure of porous membranes

or biological surfaces on a true scale.³⁻⁷ In recent years, SPT is broadly used in living systems, where analyzing the particle diffusion is highly complex because of the presence of intermolecular interactions, molecular crowding, etc.^{4, 8} SPT is also extensively used in real time imaging of protein transport in cell membranes where the protein is labeled by some fluorescent moiety.⁹

In our SPT experiments, fluorescent particles are suspended in the membrane during electrochemical formation. Tracking the movement of suspended fluorescent beads in the membrane provides the structural properties of the membrane and the viscoelastic properties of the fluid within the pores of the membrane.

The diffusion of beads in the medium depends on three different parameters:

1. size or mass of the particle,
2. viscosity and structure of the medium, and
3. temperature.

A larger or heavier particle moves more slowly at a given temperature or kinetic energy. A larger particle collides with the environment (*e.g.* solvent particles) more often than a small particle because of its larger surface, thus making the diffusion slower. In addition, the diffusion rate is highly dependent on the nature or the properties of the environment. If the environment is less viscous, diffusion occurs very rapidly because the rate of collisions is very low; the diffusion rate is slower in viscous liquids. The diffusion constant of a particle with radius r , moving in a medium with viscosity η at an absolute temperature T , can be calculated as

$$D = \frac{k_B T}{6\pi\eta r} \quad (5.1)$$

where k_B is the Boltzmann constant.^{10, 11}

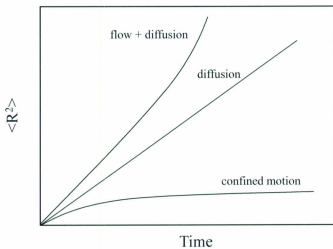


Figure 5.1: The plot of mean-square displacement, $\langle R^2 \rangle$ as a function of time has a slope which, at early times at least, equals $4D$ (as defined by Equation 5.5). The functional form at longer time varies for different motion modes. The diffusion constant D is higher for flow assisted diffusion and lower or almost zero for confined motion. Image is modified from Reference [3].

The plot of Mean Square Displacement (MSD) *vs.* time provides information about the type of mobility of a particle in a given medium. The average mean square displacement in the x direction is related to the linear drag coefficient μ by

$$\frac{\Delta \langle x^2 \rangle}{\Delta t} = \frac{2k_B T}{\mu} \quad (5.2)$$

where μ is defined as

$$\mu = 6\pi\eta a \quad (5.3)$$

With a similar expression for y , the combined MSD in two dimensions $\langle R^2 \rangle$ can be denoted as

$$\langle R^2 \rangle = \frac{4k_B T}{6\pi\eta a} t \quad (5.4)$$

which can be simplified as¹²

$$\langle R^2 \rangle = 4Dt \quad (5.5)$$

where D is the diffusion constant.^{13, 14} For our diffusion constant calculations, we use Equation 5.5 which is valid for two dimensions (x and y) because we are measuring the trajectories projected in a 2D plane. By plotting $\langle R^2 \rangle$ with time, the diffusion constant of a particle in the matrix can be calculated.

There are several modes of motion, which can be classified as anomalous diffusion, normal diffusion, tethered motion, confined motion and directed motion.³ Figure 5.1 shows how MSD ($\langle R^2 \rangle$) differs with time for different modes of motion. If the motion of the particle is through a diffusion mechanism, the MSD grows linearly with time. If flow assists particle diffusion, the effective diffusion constant is higher because the flow drags the particle faster and longer than the normal diffusion particle, resulting in higher MSD.^{10, 11}

$$MSD(t) = 4Dt + (vt)^2 \quad (5.6)$$

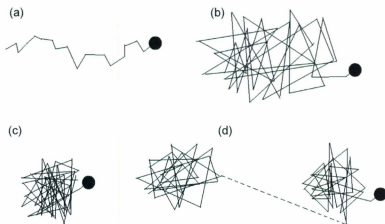


Figure 5.2: After taking hundreds of fluorescence images, the trajectories of the fluorescent bead movement in an environment can be established. Depending on parameters like pore size or matrix viscosity, the bead can move in different ways. Four different types of motion are shown here: (a) directed motion, (b) random walk, (c) confined motion and (d) intermittent or hopping random motion. Image is modified from Reference [15].

where v is the velocity of the particle.

In contrast, in confined motion, a particle moves back and forth in a restricted area, and this limited motion of the particle gives a lower MSD.¹¹

$$MSD(t) = 4Dt^\alpha \quad (5.7)$$

where α is < 1 for confined motion.

5.1.1 Trajectories for possible internal structures of membranes

The mobility of a particle in a membrane exhibits different types of trajectories depending on the internal structure of the membrane, as shown in Figure 5.2. These particle trajectories not only provide information about the type of motion, but they also illustrate the structure of the medium through which the particles are diffusing. The directed motion trajectory (Figure 5.2a) tells us that the matrix is a solution, a membrane surface, or an open channel, where there is not much restriction for the diffusion of a bead in that particular direction. Random walk (Figure 5.2b) of a particle happens mostly in solution or air where Brownian motion dominates. Brownian motion is a random motion in which the suspended particles jiggle in a random way in the medium.

A confined motion trajectory (Figure 5.2c) shows that the particle moves randomly only inside a confined region, which might be a pore or closed hole if the sample is membrane. The largest distance and the area of this confined trajectory gives a rough estimation of the size and shape of a pore in the membrane sample. The distribution, arrangement, size and shape of the pores might differ substantially for different kinds of membranes. Some of the pores might be interconnected. While tracking a particle that is trapped inside the interconnected pores, the resulting particle trajectory shows intermittent or hopping random motion, as shown in Figure 5.2d.

Table 5.1: Excitation and emission wavelengths and the supplier of various size fluorescent beads that we use for our experiments. All the beads are made of polystyrene and are stabilized by sulfate groups.^{16, 17}

Bead diameter (μm)	Excitation wavelength (nm)	Emission wavelength (nm)	Model number & Supplier
0.92	470	511	07310-15, Polysciences Inc, USA.
0.54	441	486	08691-10, Polysciences Inc, USA.
0.02	535	575	S37200, Invitrogen Mol. Probes, USA.

5.2 Methods and experimental procedure

5.2.1 Sample preparation

5.2.1.1 Preparation of fluorescent bead solutions

We use beads of various sizes (0.02 μm to 0.92 μm diameter) for our particle tracking experiments. The beads were purchased as 2.5–3 wt% aqueous solutions. The excitation and emission wavelengths and the suppliers of the beads that we have used for our experiments are given in Table 5.1. The bead solution is diluted thousands of times to get a desired bead content in the final solution. The solution is sonicated for several minutes to disperse the beads. This final solution is used to make the fluorescent-bead-containing collagen membranes.

Table 5.2: Concentration of prepared bead solution, and the concentration of beads in the final collagen monomer electrolyte for various sized beads.

Bead diameter (μm)	Concentration of added bead solution (particles/ μL)	Bead concentration in final electrolyte (particles/ μL)
0.92	18200 ± 700	1820 ± 130
0.54	14600 ± 700	1460 ± 120
0.02	28000 ± 1700	2800 ± 270

5.2.1.2 Preparation of collagen membrane incorporating fluorescent beads

To incorporate the fluorescent beads into the collagen membrane, the diluted bead solution is added in the collagen monomer electrolyte. The collagen monomer electrolyte is prepared by adding 300 μL of 3.0 mg/mL collagen monomer, ultrapure water (Barnstead, 18.2 M Ω -cm), sufficient NaOH solution (EMD Chemicals, ACS reagent grade) to bring the pH of solution to 7, and 300 μL of the desired bead solution. The added and the final concentrations of bead solutions in the collagen monomer electrolyte for various sized beads are given in Table 5.2. The concentration of bead solution in the final electrolyte is ten times lower than the original concentration of the added bead solution because the 3 mL electrolyte contains only 300 μL of bead solution.

After adding the fluorescent beads to the electrolyte, the electrolyte is sonicated to disperse the beads. Like the collagen monomers, the beads are also charged and move rapidly in the electrolyte when the potential is applied across the cell. During the collagen aggregation process, the beads are trapped inside and on the surface of the collagen membrane. After 30 minutes of applied potential, the membrane is taken out

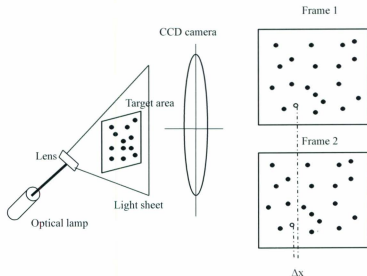


Figure 5.3: Schematic diagram of working principle of particle tracking experiment. A lens is used to convert the cylindrical light beam into a light sheet. When the sample is placed under this optical light sheet, the fluorescent particles in the sample are excited, and subsequently they emit fluorescence during relaxation. A Charge Coupled Device (CCD) camera is used to capture the fluorescence from the particles, and capturing a number of images over a given time provides an idea about the motion of the particles. By finding the positions of a particular bead in subsequent frames, the particle trajectory can be obtained. Image is modified from Reference [18].

and dried in a dark room to avoid bleaching. The membrane is re-hydrated again by adding a few drops of ultrapure water during the particle tracking experiment.

5.2.2 Instrumentation

Figure 5.3 shows the working principle of the single particle tracking method. A NIKON TE-2000 inverted microscope coupled with laser and optical light sources is used as a particle tracker. In our experiments, we use an optical lamp as an exci-

tation source, and a cylindrical lens to convert the light beam into a light sheet. A Charge-Coupled Device (CCD) camera is used to capture the images at a constant rate for a preset period. Fluorescent beads in the sample are excited by the optical light sheet, and thus give off fluorescence. This fluorescence can be seen through the microscope eye-piece or captured using the CCD camera, and appears as bright spots. Software called *Insight 3G* is used to set the parameters for camera capturing, and for post-processing of captured images.¹⁹ The capturing parameters in the software allow us to set the exposure time, capture frequency and the number of frames to be taken for a desired duration.¹⁸ Care should be taken for setting up these capturing parameters, especially the capture frequency, because a lower capture frequency leads to higher delay time that may result in missing the position of beads between successive frames. A higher capture frequency leads to a huge number of images, causing memory problems while loading the images for further analysis. For all of our experiments, the length of exposure time is 500 μs , and the capturing frequency is 2 frames per second.

5.2.3 Data analysis

To understand the motion of each and every particle, hundreds of images are taken at a preset time interval. We use the software *ImageJ* to load the frames and to convert them into a stack file.²⁰ A package called *Mosaic Plugins* is used to read the stack file, remove the background, detect the particles, and track the movement of particles between the frames.²¹ A *Perl* script reads the *ImageJ* trajectory output file, filters longer trajectories, and calculates the minimum and maximum x and y values. We read, analyze and plot the trajectories data using *IgorPro* (Wavemetrics, Lake Oswego, OR, USA). The initial x and y position values are subtracted from all frame x and y position values. For the i^{th} particle at time t , the displacements in x and y

are^{22, 23}

$$\Delta x_i(t) = x_i(t) - x_i(0) \quad (5.8)$$

and

$$\Delta y_i(t) = y_i(t) - y_i(0) \quad (5.9)$$

Therefore, the square displacement of the i^{th} particle at time t is

$$[\Delta R_i(t)]^2 = [\Delta x_i(t)]^2 + [\Delta y_i(t)]^2 \quad (5.10)$$

The mean square displacement can be obtained from

$$\langle R^2 \rangle = \frac{1}{N} \sum [\Delta R_i(t)]^2 \quad (5.11)$$

5.3 Results and discussion

5.3.1 Optimizing particle and trajectory identification

Figure 5.4a shows the fluorescence microscopy image of a fluorescent bead solution.

The bright spots in the image are due to the fluorescence emitted from the beads.

Since the number of fluorescent spots in Figure 5.4a is very large, it requires very high memory to process the image stacks, *i.e.* linking the particles and finding trajectories.

Therefore, in order to reduce the processing time and avoid memory issues, the image stacks are cropped into four quarter sections for further analysis (Figure 5.4b).

Figure 5.4a shows that the raw image is not very clear because of the background and non-uniform contrast. The background can be removed and the contrast can be adjusted using *ImageJ*. Apart from that, the data acquiring software *Insight3G* is used to enhance the intensity of the bright spots, and to suppress the background.

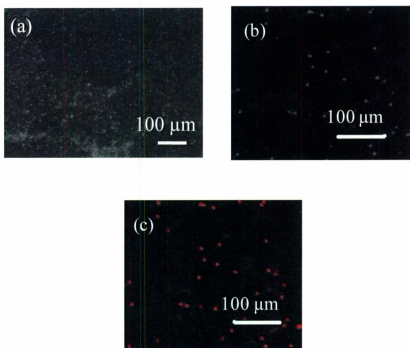


Figure 5.4: Full size (a) and cropped (b) fluorescence microscope images of a fluorescent bead solution. The bright white dots are from the fluorescent beads, and the dark gray area is the solution background. The cropped image shows fewer bright spots, and the spots are enlarged. The diameter of the fluorescent beads is $0.92 \mu\text{m}$, and the concentration of the fluorescent beads in the final electrolyte solution is $1820 \pm 130 \text{ particles}/\mu\text{L}$. (c) All the bright spots in (b) are identified correctly and circled.

There are some difficulties in the detection of exact particle positions in the images. Some particles that are underneath the membrane emit very little fluorescence, thus making it hard for the software to differentiate the particle from the background. Moreover, if the particle density is too high in the membrane, the software may miss some particles. In order to avoid these problems, it is necessary to check manually whether the software detects all the particles correctly or not. After providing some information like approximate particle radius (in pixels), cut off radius (for non-particle discrimination), and intensity percentile (that is used to decide which bright spots should be identified as particles), the software *ImageJ* detects the particles in the image and circles them. If all particles are not detected or some background is detected as a particle, changing a combination of the above three parameters allows all the particles to be identified properly (Figure 5.4c).

Once the particle detection is completed, tracking of particles over time is performed by linking the particle positions between subsequent frames. There are many complications to be dealt with while linking the particle positions into trajectories. If the particle density is too high, there might be several particles moving around in a given area. As a result, instead of detecting the position of a particular particle in subsequent frame, the software may detect another particle which floats near to it, and thus gives wrong positional values. To avoid this, it is better to use a low concentration bead solution to make the membrane, so that the presence of few particles in a small area makes it easier to track them for a longer period. Additionally, linking the particle position between frames depends on the type of motion. The particles may move by free diffusion in a fluid, confined motion if the volume is very small, or a long distance with a high speed if the particles are dragged by an applied external force. For that reason, it is essential to feed the approximate linker length (in pixels) between the frames to make sure that the software connects the same particle in the

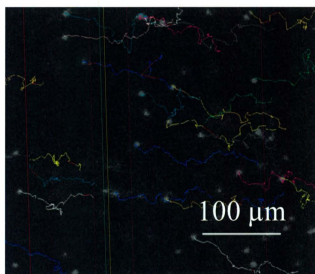


Figure 5.5: Trajectories of fluorescent beads in solution. Different colored trajectories show the motion of different fluorescent beads in both x and y directions.

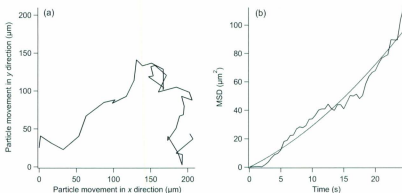


Figure 5.6: (a) Trajectory of a fluorescent bead in solution shows that the motion of the bead is a random walk, and the bead can move in any direction between the frames. (b) Mean square displacement (MSD) vs. time plot for a fluorescent bead in solution. This curve is fitted against Equation 5.6 and the obtained D and v are $0.55 \mu\text{m}^2/\text{s}$ and $0.26 \mu\text{m}/\text{s}$ respectively.

subsequent frame rather than connecting it with another particle.

Figure 5.5 shows the trajectories of fluorescent bead particles ($0.92 \mu\text{m}$ diameter) in water. The trajectories are obtained by connecting the x and y positions of each particle in all frames. As shown in Figure 5.2a, the shape of the trajectories illustrates that the particles move by flow or directed motion.

5.3.2 Validating the setup: particle tracking in water

Trajectory plots provide information about the type of mobility of a particle in a medium, *i.e.* whether it is Brownian diffusion, directed motion or confined motion. In addition, the mean square displacement (MSD) of particle trajectories can be calculated and plotted against time to get more information such as diffusion constant and pore-liquid viscosity.

Most of the trajectories in the Figure 5.5 show directionality in the particle motion, perhaps from solvent evaporation or from convective heating. Figure 5.6a shows that

the motion of bead in solution is directed: the bead tends to move in a particular direction (toward the right). We have calculated the MSD values for each trajectories and plotted them with time as shown in Figure 5.6b. The curves are fitted against Equation 5.6, by using that we can determine the diffusion constant, D and velocity, v of the diffusing particle.²⁴ The calculated D and v for $0.92 \mu\text{m}$ beads in water are $0.53 \pm 0.19 \mu\text{m}^2/\text{s}$ and $0.24 \pm 0.09 \mu\text{m}/\text{s}$ respectively. The D value is of the same magnitude as the theoretically calculated D ($0.48 \mu\text{m}^2/\text{s}$) using Equation 5.1. This value is also similar to the literature D values of 0.40, 0.43 and $0.48 \mu\text{m}^2/\text{s}$ that are reported for 1.02, 0.98 and $0.97 \mu\text{m}$ spheres in water, respectively.^{14, 25}

5.4 Pore-size analysis for collagen membranes

Figure 5.7 shows the fluorescence microscope image of a collagen membrane prepared with the addition of $0.92 \mu\text{m}$ fluorescent beads in the electrolyte. It shows that the beads do not disperse in the same way throughout the membrane. In some regions of the membrane, the individual beads spread well throughout the membrane, and in some regions, the beads are clumped together.

For a clear view of the beads and for processing convenience, the image in Figure 5.7 is cropped into four quarter sections as shown in Figure 5.8a. The trajectories of fluorescent beads are very small in length (shown as colored dots in Figure 5.8b), because the beads move very small distances. The single particle trajectory plot (Figure 5.9a) not only gives information about the type of motion; it also gives knowledge about the membrane pore structure like pore diameter/area and shape. Since the beads move only inside the pores of the membrane, the beads can visit almost all corners of the membrane pores in 250 seconds. Therefore, the entire trajectory gives the shape and dimensions of that particular pore. From Figure 5.9a, it can be concluded that

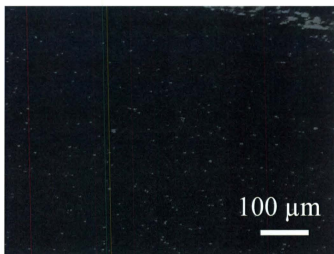


Figure 5.7: Fluorescence image of a collagen membrane in which $0.92 \mu\text{m}$ fluorescent beads are incorporated. The bright spots are from the fluorescent beads, and the black or gray area is the collagen membrane. The image shows that the beads are dispersed well, and individual beads are clearly visible everywhere in the membrane except in a few areas where several beads are aggregated in clusters (see the top-right corner of the image).

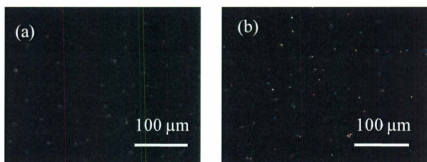


Figure 5.8: (a) Cropped image of Figure 5.7. (b) Trajectories of $0.92 \mu\text{m}$ beads in the collagen membrane.

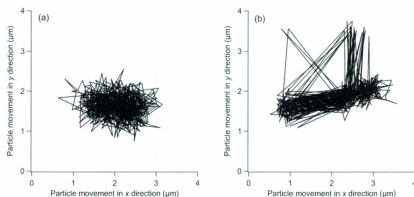


Figure 5.9: Particle trajectories of (a) $0.92 \mu\text{m}$ and (b) $0.54 \mu\text{m}$ beads in a collagen membrane show that the particles move randomly in the pores of membrane, and that the size of the pore is $2\text{--}3 \mu\text{m}$.

the pore is ovoid shaped with a mean diameter of $2\text{--}5 \mu\text{m}$.

Table 5.3 shows the pore size and area values for $0.92 \mu\text{m}$ fluorescent beads added to a collagen membrane. Since the beads move back and forth only inside the pores of the membrane, the minimum and maximum x and y values of the bead trajectories give the approximate pore diameter. The bead diameter value is added to the trajectory-obtained value to get the original pore size, because in a $4 \mu\text{m}$ pore, the center of the $1 \mu\text{m}$ bead can move only $3 \mu\text{m}$. Table 5.3 shows that the dimensions of most of the pores are similar throughout the membrane. The estimated pore diameter is approximately $3\text{--}6 \mu\text{m}$ and the area is $7\text{--}14 \mu\text{m}^2$, if we consider the shape of the pore as a polygon. Though only a few trajectory results are shown in the Table 5.3, more than 40 trajectories are included for the pore size and area calculations.

To verify the pore size/area calculations, we performed the particle tracking experiments for the collagen membranes prepared with 0.54 and $0.02 \mu\text{m}$ size beads as well. Figure 5.9b shows the particle trajectory plot for $0.54 \mu\text{m}$ bead in a pore of a collagen membrane. In the case of $0.54 \mu\text{m}$ beads, the pore size and area that are calculated

Table 5.3: Pore size and pore area calculation for selected trajectories in the collagen membrane prepared with $0.92 \mu\text{m}$ fluorescent beads. The minimum and maximum x and y values in the trajectory plot (Figure 5.9a) are used to calculate the approximate pore diameter in the x and y directions and approximate pore area. The bead diameter ($0.92 \mu\text{m}$) is added to the trajectory-obtained value to get the original pore size. Multiple trajectories give information about different pores in the membrane.

Trajectory No	Pore size in x μm	Pore size in y μm	Pore Area μm^2
1	3.0	2.9	7.1
2	4.3	2.7	10.2
3	4.1	3.9	14.7
4	5.1	3.2	14.8
5	4.0	3.5	12.6
6	3.5	2.8	8.4
7	3.9	2.9	9.9
8	4.8	2.7	11.5
9	3.4	2.9	8.5
Average	4.0 ± 0.7	3.1 ± 0.4	10.9 ± 2.8

Table 5.4: T-test comparisons for the pore areas of various collagen membranes.

Set I	Set II	Pore area (μm^2)		Probability (P)
		Set I	Set II	
Col+0.92 μm	Col+0.54 μm	10.9	13.4	0.22
Col+0.92 μm	Col+0.02 μm	10.9	25.7	0.05
Col+0.92 μm	Col+0.92 μm + CaCl ₂	10.9	21.7	0.002
Col+0.92 μm	Col+0.92 μm + KCl	10.9	8.3	0.1

from several trajectory plots are 4–7 μm and 10–22 μm^2 respectively. On the other hand, for the collagen membrane prepared with 0.02 μm beads, the estimated pore size is approximately 4–10 μm and the area is 20–35 μm^2 .

T-tests were carried out (using *R Gui*²⁶) to compare the distribution of pore sizes within a membrane to the distribution between the membranes (Table 5.4). The results show that the obtained pore area values are in the similar range if either 0.94 μm or 0.54 μm beads are used, and the probability for these two pore area values to be similar is 0.22. On the other hand, using much smaller beads (0.02 μm) provides a slightly larger pore area, and the t-test probability is 0.05 for this value to be equal with the pore area calculated using 0.94 μm beads.

The estimated pore size and pore area of the collagen membrane are larger if we use smaller (0.54 μm , 0.02 μm) beads for the measurement because small beads can move efficiently inside the pores and can reach all the corners of pores more easily than larger beads.

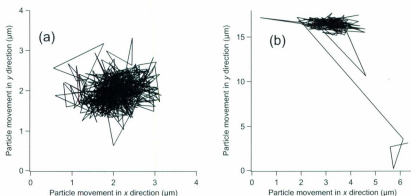


Figure 5.10: Particle trajectories of $0.92 \mu\text{m}$ beads in a collagen membrane that is prepared with the addition of 0.05 M KCl . Trajectory (a) shows that the beads move randomly inside the pores of collagen membrane. Moreover, the pore sizes ($2\text{--}5 \mu\text{m}$) are similar to the pore sizes of the regularly prepared collagen membrane. Trajectory (b) shows that some membrane pores are interconnected such that a bead can escape from one pore and get into another pore.

5.4.1 Pore shapes/interconnectedness

As we know from Chapter 2, the presence of additional ions like Ca^{2+} , Na^+ , and K^+ in the electrolyte form a membrane with different mechanical and structural properties. Here, we have used the particle tracking method to analyze how the pore structures differ for the membranes prepared with and without these additional ions.

Figure 5.10 shows the mobility of fluorescent particles in pores of a collagen membrane, which is prepared with the addition of 0.05 M KCl in the electrolyte during the electrochemical assembly process (softer membrane). Most of the trajectories obtained for this sample do not differ much from the trajectories that are obtained for the normal (no added K^+) collagen membrane. For example, Figure 5.10a looks similar to the trajectories of the normal membrane. The estimated pore size and pore area of this membrane are $4\text{--}6 \mu\text{m}$ and $8\text{--}15 \mu\text{m}^2$ (measured from 40 trajectories), which are similar to the pore dimensions of collagen membranes prepared without addition of

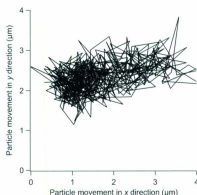


Figure 5.11: Particle trajectory of $0.92 \mu\text{m}$ bead in a collagen membrane prepared with the addition of 0.05 M CaCl_2 shows that the particle moves randomly in membrane pores, and the size of the pore is $\sim 4.5 \mu\text{m}$ including the diameter of the bead.

KCl. T-tests also show that the pore area of normal and softer membrane (prepared with KCl) lie in the same distribution with the probability of 0.1 (Table 5.4). On the other hand, some trajectories show that the fluorescent beads move inside a pore for some time and then escape to another pore and start moving in that pore (Figure 5.10b). This suggests that some pores are interconnected in the collagen membrane which is prepared with the addition of KCl.

The trajectory of the movement of $0.92 \mu\text{m}$ fluorescent bead in the collagen membrane prepared with the addition of 0.05 M CaCl_2 (harder membrane) is shown in Figure 5.11a. The type and the shape of the trajectories show that the pore size and area of the harder membrane are larger than the pores of normal collagen membrane. The t-test probability for the pore areas of normal and stiffer collagen membranes to be similar is 0.002, which indicates that pore area the values are significantly different for these two membranes. The calculated pore size and area values for the membranes prepared with and without added ions are given in Table 5.5.

Table 5.5: Summary of the pore size and pore area calculations done using different size beads for various collagen membranes prepared with and without addition of KCl or CaCl_2 salts. The table shows that the pore size and area are similar for normal and softer membranes, and the pores are larger for the stiffer membrane. Small beads give larger pore values because they can move efficiently inside the pores and can reach all the corners of pores more easily than larger beads. SD denotes standard deviation.

Sample	Pore size in x	Pore size in y	Pore area
	average (SD)	average (SD)	average (SD)
	μm	μm	μm^2
Col+0.02 μm	8.8 ± 1.3	4.3 ± 0.7	25.7 ± 8.6
Col+0.54 μm	4.3 ± 1.2	3.7 ± 0.8	13.4 ± 5.6
Col+0.92 μm	3.8 ± 0.8	4.1 ± 1.2	10.9 ± 2.7
Col+0.92 μm +KCl	3.7 ± 0.9	3.9 ± 1.0	8.3 ± 3.0
Col+0.92 μm + CaCl_2	6.5 ± 1.0	4.7 ± 0.9	21.7 ± 8.7

Table 5.6: Diffusion constant and membrane pore-liquid viscosity calculations performed using different size beads for the collagen membranes prepared with and without addition of KCl or CaCl_2 salts. The smaller beads diffuse well in the pores of the collagen membrane, thus giving higher D values. The diffusion constant is calculated from the slope of MSD *vs.* time plots (Figure 5.12), and the viscosity is calculated using Equation 5.1.

Sample	Diffusion Constant ($\times 10^{-6} \mu\text{m}^2/\text{s}$)	Viscosity at 20 °C (Pa·s)
Col+0.02 μm	86.0 ± 12.8	249 ± 35
Col+0.54 μm	17.0 ± 8.0	46 ± 20
Col+0.92 μm	6.4 ± 1.7	72 ± 20
Col+0.92 μm +KCl	6.9 ± 3.8	67 ± 25
Col+0.92 μm + CaCl_2	13.0 ± 6.7	35 ± 15

5.4.2 Diffusion constants and membrane pore-liquid viscosities

Figures 5.12a and b show the MSD *vs.* time plot of 0.92 μm and 0.54 μm bead trajectories in a collagen membrane. The slope of a linear fit in the MSD *vs.* time plot corresponds to $4D$ in Equation 5.5. The average diffusion constant, D , calculated from 40 trajectories for the mobility of 0.92 μm beads in collagen membrane pores is $6.4 \pm 2.0 \times 10^{-6} \mu\text{m}^2/\text{s}$. Table 5.6 summarizes the diffusion constants calculated from data for various sized beads in different types of membranes. As expected, the diffusion constant values are higher for smaller beads since smaller beads diffuse faster than larger beads in the same environment (according to Equation 5.1). All

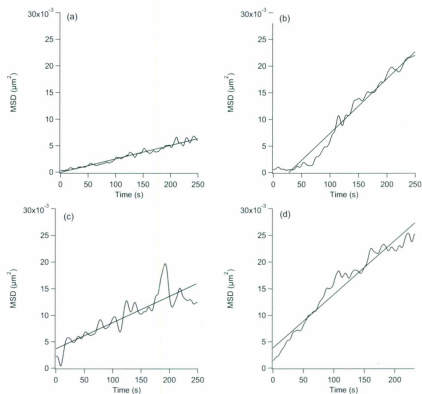


Figure 5.12: MSD vs time plots of (a) $0.92 \mu\text{m}$ and (b) $0.54 \mu\text{m}$ beads in the pores of a collagen membrane. MSD vs. time plot for the motion of a $0.92 \mu\text{m}$ bead in a collagen membrane prepared with the addition of (c) 0.05 M KCl or (d) 0.05 M CaCl_2 .

Table 5.7: T-test comparisons for the liquid viscosities (η) in the pores of normal, softer and stiffer collagen membranes.

Set I	Set II	η (Pa-s)		Probability (P)
		Set I	Set II	
Col+0.92 μm	Col+0.92 μm + KCl	72	67	0.7
Col+0.92 μm	Col+0.92 μm + CaCl ₂	72	35	0.008

of the calculations performed for various collagen membranes show that the diffusion constant values are much lower for the beads inside the membrane pores than they would be in water. That is because compared to water, the viscosity of the fluids in the pores of collagen membrane is much higher (Table 5.6). Table 5.6 shows the viscosity (η) of the solution in the pores of different collagen membranes, calculated using Equation 5.1, assuming that the manufacturer-supplied particle radius is the hydrodynamic radius and the temperature is 20 °C. Table 5.7 shows that the viscosities of the pore-liquids do not differ substantially between normal and softer membranes (prepared with KCl), which is also confirmed by the higher probability of t-test ($P \sim 0.7$). On the other hand, the viscosity of the pore-liquid in stiffer membrane (prepared with CaCl₂) is lower than the viscosity of pore-liquid in normal or softer membranes. The lower t-test probability value (0.008) also indicates that the viscosity values differ considerably between normal and stiffer membranes. We attribute the higher viscosities to the presence of monomers in the pore-liquid. Thus the higher monomeric contents in the normal and softer membranes make their pore-liquids more viscous than the pore-liquid of stiffer membranes.

5.5 Conclusions

In this chapter, I have shown that we can use the simple and widely used particle tracking technique for the analysis of the internal structure of electrochemically aggregated collagen membranes. First, I have performed the experiment for the bead solutions (no collagen or salt) to validate our experimental setup and diffusion constant calculations. The obtained trajectories and the calculated D values for the bead solutions show that although the diffusion of beads in solution has a component of directed motion, the obtained diffusion constant values are generally consistent with theoretical and literature values. The analysis of internal pore structure and area for the collagen membrane using various sized fluorescent beads shows that the size, shape and area of most of the pores are similar throughout the membrane. In addition, we found that the pore structures vary somewhat between the harder (the membrane prepared with Ca^{2+} ions) and softer (the membrane prepared with K^{+} ions) collagen membranes, and some pores are interconnected in the softer membrane. The pore-liquid viscosities, η in the normal and softer collagen membranes are in the same range and are lower in the stiffer membrane due to its lower monomeric content.

References

- [1] Haramagatti, C. R.; Schacher, F. H.; Müller, A. H. E.; Köhler, J. *Phys. Chem. Chem. Phys.* **2011**, *13*, 2278–2284.
- [2] Ragan, T.; Huang, H.; So, P.; Gratton, E. *J. Fluoresc.* **2006**, *16*, 325–336.
- [3] Saxton, M. J.; Jacobson, K. *Annu. Rev. Biophys. Biomol. Struct.* **1997**, *27*, 373–399.
- [4] Jin, S.; Haggie, P. M.; Verkman, A. S. *Biophys. J.* **2007**, *93*, 1079–1088.

- [5] Levi, V.; Gratton, E. *Cell. Biochem. Biophys* **2007**, *48*, 1–15.
- [6] Babcock, H. P.; Chen, C.; Zhuang, X. *Biophys. J* **2004**, *87*, 2749–2758.
- [7] Manley, S.; Gillette, J. M.; Jennifer, L.-S. *Methods in Enzymology* **2010**, *475*, 109–120.
- [8] Douglass, A. D.; Vale, R. D. *Cell* **2005**, *121*, 937–950.
- [9] Alcor, D.; Gouzer, G.; Triller, A. *Eur. J. Neurosci.* **2009**, *30*, 987–997.
- [10] Qian, H.; Sheetz, M. P.; Elson, E. L. *Biophys. J.* **1991**, *60*, 910–921.
- [11] Morrison, Jennifer, S. *Deciphering multi-state mobility within single particle trajectories of proteins on the plasma membrane*, Thesis, The University of British Columbia, 2010.
- [12] Kumar, A.; Gorti, V. M.; Shang, H.; Lee, G. U.; Yip, N. Kand Wereley, S. T. *J. Fluids. Eng.* **2011**, *130*, 111401.
- [13] Ekani-Nkodo, A.; Kuchmir Fygenon, D. *Phys. Rev.* **2003**, *67*, 021909.
- [14] Crocker, J. C. *J. Chem. Phys.* **1997**, *7*, 2837–2840.
- [15] Saxton, M. J. *Nature Methods* **2008**, *5*, 671–672.
- [16] “<http://www.polysciences.com>”, Last accessed on November 2011.
- [17] “<http://products.invitrogen.com>”, Last accessed on November 2011.
- [18] “<http://www.dantecdynamics.com/Default.aspx?ID=454>”, Last accessed on August 2011.
- [19] “Insight 3G, Data Acquisition, Analysis, and Display Software Platform, User’s Guide: Trust Science Innovation”, 2004.

- [20] "ImageJ is available for free at <http://www.macbiophotonics.ca/imagej/>", Last accessed on August 2011.
- [21] Sbalzarini, F.; Koumoutsakos, P. *J. Struct. Biol* **2005**, *151*, 182–195.
- [22] Nakroshis, P.; Amoroso, M.; Legere, J.; Smith, C. *Am. J. Phys* **2003**, *71*, 568–573.
- [23] Crocker, J. C.; Hoffman, B. D. *Methods. Cell. Biol.* **2007**, *83*, 141–178.
- [24] Salmon, R.; Robbins, C.; Forinash, K. *Eur. J. Phys* **2002**, *23*, 249–253.
- [25] Oppong, F. *Probing the microstructure of yield-stress fluids using multiple particle tracking*, Thesis, Memorial University of Newfoundland, 2005.
- [26] "R Gui is available for free at <http://cran.r-project.org/bin/windows/base/>", Last accessed on November 2011.

Chapter 6

Conclusions

6.1 Summary

Electrochemical aggregation is a viable method to align synthetic collagen structures with some degree of orientational anisotropy and hence with some control of mechanical properties. We chose an electrochemical method to aggregate the collagen membranes because process variables like *pH*, concentration, and duration can be altered easily. Furthermore, since the approaches described here do not use harsh (thermal or toxic solvent based) synthetic methods, the prepared membranes retain their original nature and bioactivity. Several drawbacks of conventional methods (coating, extrusion, physical vapor deposition and electro-spinning process) including poor mechanical strength, poor biocompatibility and improper alignment have been overcome by our electrochemical method.

To characterize our collagen membrane samples, we use Raman and infrared spectroscopies (internal structure and aggregate type), atomic force microscopy (nanoscale morphology), UV-visible spectroscopy (monitoring protein content in electrolyte over time) and force spectroscopy (stiffness). The results show that changes in electrolyte

composition (by adding different ions), electrolyte pH, or duration of the applied field produce membranes with a range of Young's moduli. The presence of Ca^{2+} , Ba^{2+} and Na^+ in the electrolyte increases the stiffness of the membranes. On the other hand, Mg^{2+} and K^+ decrease the stiffness of the aggregated collagen membrane. Atomic force microscopy and Raman spectroscopy reveal that the change in Young's modulus is related to the fibril content of the membrane. The membranes with higher stiffness show higher fibril content compared to the membranes that show lower stiffness.

The ion-induced change in membrane stiffness or fibril content is attributed to the aggregation pathway. In general, aggregation from a monomer solution can follow a specific path leading to robust fibrils. Non-specific aggregation does not lead to any fibril formation. The presence of excess ions in the electrolyte can change the pathway of the membrane aggregation process, thus leading to a change in stiffness. In addition, increasing the electrochemical process duration (or applied potential duration) increases the Young's moduli by increasing the fibril content. Though pH is the main factor in the isoelectric focusing aggregation process, the initial electrolyte pH does not have any effect on the fibril content, internal structure and Young's moduli of the assembled collagen membranes.

We can further relate the changes in mechanical properties to the pore structure of the membrane. We used single particle tracking (SPT) to assess the pore size/area and structure of our electrochemically aggregated collagen membranes. The pore size is higher for the harder collagen membranes (prepared with the addition of Ca^{2+}) than the normal and softer membranes. In the softer collagen membrane (prepared with K^+), some pores are interconnected. The pore-liquid viscosities in the normal and softer collagen membranes are in same range, but lower in the stiffer membrane due to its lower monomeric content.

The electrochemically aggregated collagen membranes show suitable characteristics

for use as a matrix in an artificial cornea. The collagen membrane has a higher denaturation temperature than the body temperature or monomeric collagen; hence, body heat would not affect the membrane structure if used as a matrix for artificial cornea. The electrochemically aggregated collagen membranes can transmit more than 90% of visible light, which is another important feature if these collagen membranes are to be used as a matrix for artificial corneas. The biocompatibility studies that are carried out at the School of Medicine, Memorial University, show that MK/T-1 cornea fibroblast cells grow very well and move actively when they are incubated with the collagen matrix. Furthermore, the presence of the collagen matrix in the cell culture medium keeps the cells in a quiescent state, another necessary requirement for use in artificial cornea.

These collagen matrices can also be mineralized for use in applications where a bone-like material is required. Synthesis of collagen-calcium phosphate membranes involves two steps: assembly of the collagen membrane from aqueous solutions, and then precipitation of a calcium phosphate layer on it. IR, Raman and EDX spectroscopies show that for most of the collagen-calcium phosphate composite membranes, the obtained mineral phase is carbonated hydroxyapatite. In addition, experiments performed with and without collagen in the electrolyte show that collagen helps to nucleate the growth of calcium phosphate. The electrochemically precipitated collagen-calcium phosphate membranes could be applied over a ruptured bone so that the mineral calcium phosphate supports the bone while the protein collagen assists the bone cells to grow. In fact, the use of a biocompatible implant for curing an injury could reduce the pain and improve the healing process for the patient.

6.2 Future directions

The fields of collagen and collagen-calcium phosphate composites are huge, so there are many possibilities for one to do more innovative research to develop new materials and characterize them, or tailor the existing materials for various applications.

Though we have found that electrolyte composition affects the internal structure, pore structure and mechanical properties of the formed collagen membranes, it would be a great idea to uncover the mechanism behind it. It could be possible to use theoretical models to investigate how the presence of various ions impact the nanomechanics of collagen. For example, Buehler¹ used molecular dynamics simulations to understand the nanomechanics of collagen during a fracture or under an applied load. The results show that the length of the tropocollagen molecules and their intermolecular interactions are the two vital parameters that influence the fracture mechanics. In the same way, one could compare his results with a similar model that includes ions in the simulation.

Even though the mechanical properties and pore structures of various membranes are characterized well in this thesis work, there are still some puzzles in relating the mechanical properties with the pore structure of the membrane. Quinn *et al.*² have used finite element modeling to calculate the contributions of density and orientation of collagen fibrils in the mechanics of cartilage. One could characterize the structure and dynamics of the membranes³ using solid-state NMR. ³¹P and ¹³C solid-state NMR coupled with magnetic resonance imaging (MRI) has been used by Weber *et al.*⁴ for the quantitative investigation of the synthesis of collagen and biomineral (apatite) in a polymer based bone implant material. ¹³C NMR spectroscopy characterizes the formation of collagen in the scaffold material, while the ³¹P characterizes the formation of apatite minerals. In addition, solid-state NMR has been used by others to analyze the hydration or temperature effects on the internal dynamics of collagen.^{5, 6}

Since our cell culture studies have proven that the collagen membrane controls the cell growth, one may use these membranes to study how different kinds of cells behave in a given micro-environment (*i.e.*, using the collagen membrane as a tool to study cell biology). The effects of matrix stiffness on the growth of cells have been widely studied because the matrix tissue stiffness plays a key role in deciding the cell functions, and any change in tissue stiffness can lead to cancer or disease.^{7, 8} Finding alternate ways to make the membranes with a range of elastic moduli (like exposing to UV radiation, cross-linking with polylactic acid⁹ or glutaraldehyde¹⁰) would be an interesting way to do further research if addition of excess ions gives some negative effect. Cretu *et al.*⁸ used a hydrogel as an extracellular matrix for cell culture, and AFM was used to analyze the stiffness of the matrices. Matrices were prepared with various stiffnesses by changing the percentage of monomer solutions during polymerization. They found that the cells respond differently when they are cultured in various stiffness matrices. Mitrossilis *et al.*¹¹ monitored the response of a cell in real time for an applied external force, which shows that cells adapt to the applied external force in less than 0.1 s. Moreover, an increase in the extracellular matrix rigidity can reduce the cell proliferation (DNA replication) on the matrix.¹²

References

- [1] Buehler, M. J. *Proc. Natl. Acad. Sci. USA* **2006**, *103*, 12285–12290.
- [2] Quim, T. M.; Morel, V. *Biomechan. Model. Mechanobiol* **2007**, *6*, 73–82.
- [3] Huster, D. *Annu. Rep. NMR Spectrosc* **2008**, *64*, 127–159.
- [4] Weber, F.; Bohme, J.; Scheidt, H. A.; Grunder, W.; Rammelt, S.; Hacker, M.; Schulz-Siegmund, M.; Huster, D. *NMR. Biomed* **2011**, DOI: 10.1002/nbm.1649.

- [5] Torchia, Dennis, A. *Ann. Rev. Biophys. Bioeng.* **1984**, *13*, 125–144.
- [6] Reichert, D.; Pascui, O.; deAzevedo, E. R.; Bonagamba, T. J.; Arnold, K.; Huster, D. *Magn. Reson. Chem* **2004**, *42*, 276–284.
- [7] Discher, D. E.; Janmey, P.; Wang, Y. L. *Science* **2005**, *310*, 1139–1143.
- [8] Cretu, A.; Castagnino, P.; Assoian, R. *J. Vis. Exp.* **2010**, *10*, pii: 2089. doi: 10.3791/2089.
- [9] Liao, S. S.; Guan, K.; Cui, F.; Shi, S.; Sun, T. *Spine* **2003**, *28*, 1954–1960.
- [10] Kikuchi, M.; Matsumoto, h. N.; Yamada, T.; Koyama, Y.; Takakuda, K.; Tanaka, J. *Biomaterials* **25**, 2004, 63–69.
- [11] Mitrossilis, D.; Fouchard, J.; Pereira, D.; Postic, F.; Richert, A.; Saint-Jean, M.; Asnacios, A. *Proc. Natl. Acad. Sci. USA.* **2010**, *107*, 16518–16523.
- [12] Lam, W.; Cao, L.; Umesh, V.; Keung, A. J.; Sen, S.; Kumar, S. *Molecular Cancer* **2010**, *9*, 2–7.

Appendix A

Studying the effects of different cations on structure and mechanical properties *

Our investigations show that adding different ions to the electrolyte have dramatically different effects on the stiffness of the resulting collagen scaffold, suggesting that ion content in the electrolyte has a strong effect on the collagen assembly process. Earlier work has shown that Ca^{2+} increases stiffness, K^+ decreases stiffness and Na^+ has a minimal effect¹ (Chapter 2). This may be because Ca^{2+} and Na^+ support fibril growth in the membrane, while K^+ leads to fibril growth in the electrolyte rather than assisting the fibril growth in the membrane. Atomic force microscopy (AFM) images of collagen membranes that are prepared with the addition of Ca^{2+} and Na^+ (Figure A.1b,c) show that these membranes contain a large number of fibrils, which

¹Some of these data are published in "A Role for Electrochemical Synthesis in Bioceramic Composite Materials" M. Ramesh Kumar, Erika F. Merschrod S., Kristin M. Poduska, *Ceramic Transactions* **2011**, 218 3–13.

The candidate contributed to experimental design, collected and analyzed all data, contributed to the revision of the manuscript, and wrote this appendix.

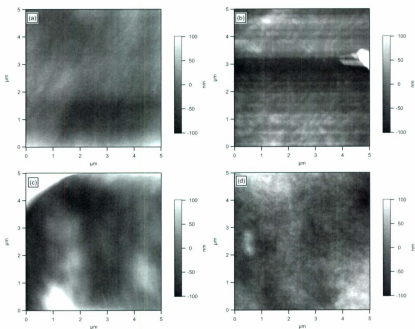


Figure A.1: Atomic Force Microscopy (AFM) images of collagen membranes prepared with and without the addition of excess ions. (a) AFM image of a collagen membrane prepared without any added salt shows no fibrils. AFM images of the collagen membranes prepared with (b) Ca^{2+} or (c) Na^{+} show fibrils. (d) K^{+} ions in the electrolyte do not lead to fibril formation in the membrane.

proves that addition of these ions helps the fibrils to grow well in the membrane. In contrast, the collagen membrane prepared with K^{+} does not show any fibril content (Figure A.1d), which is because addition of K^{+} in the electrolyte leads to fibril growth in the electrolyte rather than assisting fibril growth in the membrane. Moreover, the collagen membranes prepared without the addition of any of these salts do not show any fibril content (Figure A.1a).

In Chapter 2 it is stated that increasing the duration of applied potential can lead to a highly matured collagen membrane with higher elastic modulus, and the quantity of collagen in the electrolyte decreases with applied potential duration (electrochemi-

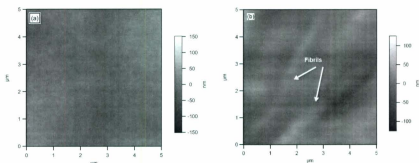


Figure A.2: AFM images of collagen membranes prepared with different applied potential durations. (a) Collagen membrane prepared with an applied potential duration of 15 minutes does not have any fibrils. (b) AFM image of a collagen membrane prepared with an applied potential duration of 60 minutes shows many fibrils.

cal process duration).¹ AFM images for the membranes prepared for various applied potential durations (15 and 60 minutes) prove that when the electrochemical process duration increases, more fibrils are found in the membrane (Figure A.2). The membrane prepared for less time does not contain fibrils, while fibrils are clearly visible in the membrane prepared for longer times (Figure A.2).

Moreover, we found that adding different doubly charged cations to the electrolyte can make either stiffer or softer films, as shown in Figure A.3. Addition of Ba^{2+} in the electrolyte makes the membrane stiffer (as with Ca^{2+}), and addition of Mg^{2+} makes the membrane softer (like K^+).²

The addition of various chloride salts (CaCl_2 , NaCl and KCl) in the electrolyte produces collagen membranes with different stiffness values, which suggests that the cations play a role in changing the stiffness, not the Cl^- anion. To verify the above statement, we also prepared collagen membranes by adding different concentrations of $\text{Ca}(\text{NO}_3)_2$. The stiffness calculations that are performed for these collagen membranes show that the stiffness value increases with the concentration of $\text{Ca}(\text{NO}_3)_2$, as

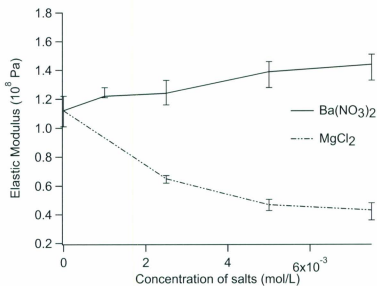


Figure A.3: Elastic moduli values can change dramatically with the addition of different concentrations of ions such as Mg^{2+} or Ba^{2+} during membrane formation. The presence of Ba^{2+} in the electrolyte increases the elastic modulus value, and presence of Mg^{2+} in the electrolyte decreases the elastic modulus of the collagen membrane.

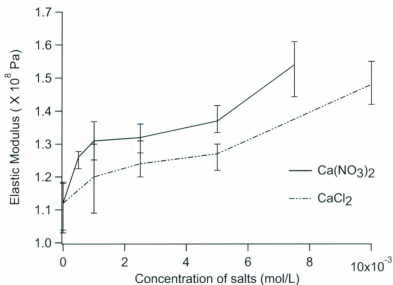


Figure A.4: Young's modulus values for the collagen membranes prepared with various concentrations of CaCl_2 and $\text{Ca}(\text{NO}_3)_2$. As with CaCl_2 , the Young's modulus also increases with the concentration of $\text{Ca}(\text{NO}_3)_2$, which suggests that the cation Ca^{2+} plays a role in increasing the Young's modulus value, not the anion Cl^- . In fact, the nitrate salt increases the stiffness further because its additional electrochemical activity accelerates pH gradient formation.

it does for CaCl_2 (Figure A.4). We observed that there are no correlations for the change in elastic moduli with the valency or size/charge density of added metal ions.

References

- [1] Kumar M. R.; Merschrod S., E. F.; Poduska, K. M. *Biomacromolecules* **2009**, *10*, 1970–1975.
- [2] Kumar, M. R.; Merschrod S., E. F.; Poduska, K. M. *Ceram. Trans* **2010**, *218*, 3–13.

Appendix B

Collagen-hydroxyapatite *vs.* collagen-brushite composites *

From our infrared (IR) studies, we know that K_2HPO_4 , KH_2PO_4 , and NaH_2PO_4 precursors produce hydroxyapatite in the presence of collagen with either $CaCl_2$ or $Ca(NO_3)_2$. On the other hand, another phosphate salt ($NH_4H_2PO_4$) gives brushite with $CaCl_2$ and hydroxyapatite with $Ca(NO_3)_2$ when they react electrochemically in the presence of collagen¹ (Chapter 3). To confirm our IR results, we also carried out Raman spectroscopy analyse (collected with 532 nm excitation from a confocal Jobin Yvon Horiba, LabRAM) for all the collagen-calcium phosphate membranes prepared using various calcium and phosphate salts. Figure B.1a shows the Raman spectra of collagen-calcium phosphate composites prepared with $CaCl_2$ and three different phosphate salts. These spectra show that $CaCl_2$ gives hydroxyapatite when it reacts with either K_2HPO_4 or KH_2PO_4 , and gives brushite when reacting with $NH_4H_2PO_4$.

¹Some of this data is published in "A Role for Electrochemical Synthesis in Bioceramic Composite Materials" M. Ramesh Kumar, Erika F. Merschrod S., Kristin M. Poduska, *Ceramic Transactions* **2011**, 278 3-13.

The candidate contributed to experimental design, collected and analyzed all data, contributed to the revision of the manuscript, and wrote this appendix.

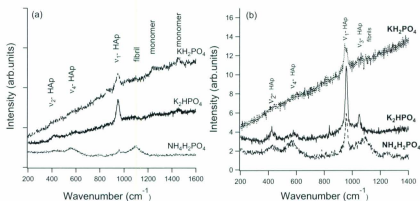


Figure B.1: Raman spectra for layered calcium-phosphate composites prepared from one of three different phosphate salts (K_2HPO_4 , KH_2PO_4 , or $\text{NH}_4\text{H}_2\text{PO}_4$) and (a) 10 mM CaCl_2 or (b) 10 mM $\text{Ca}(\text{NO}_3)_2$. Peaks indicative of hydroxyapatite (labeled HAp) and collagen (labeled fibril or monomer) are evident in all samples, except the one that is prepared with CaCl_2 and $\text{NH}_4\text{H}_2\text{PO}_4$, in which the obtained mineral phase is brushite. Spectra are offset along the intensity axis for clarity, and peak assignments are based on previous studies.³⁻⁵

If $\text{Ca}(\text{NO}_3)_2$ is used instead of CaCl_2 , the obtained mineral phase is hydroxyapatite for all three phosphate salts (Figure B.1b).²

An energy dispersive X-ray diffractometer (Röntec EDX, software from JKTech, University of Queensland Australia) is used to analyze the various calcium phosphate phases that are present in the collagen-calcium phosphate membranes. Figure B.2a shows the EDX spectrum of a collagen-calcium phosphate membrane that is prepared with the addition of collagen, CaCl_2 and K_2HPO_4 . The intensity ratio between the Ca and P is 1.6, which is consistent with hydroxyapatite which has a Ca : P ratio of 1.67 ($\text{Ca}_{10}(\text{PO}_4)_6(\text{OH})_2$).^{6,7} Figure B.2b shows the EDX spectrum of a collagen-calcium phosphate membrane prepared with the addition of collagen, CaCl_2 and $\text{NH}_4\text{H}_2\text{PO}_4$. The intensity ratio between Ca and P is 0.9, which suggests that the obtained mineral phase is brushite ($\text{CaHPO}_4 \cdot 2\text{H}_2\text{O}$).⁸

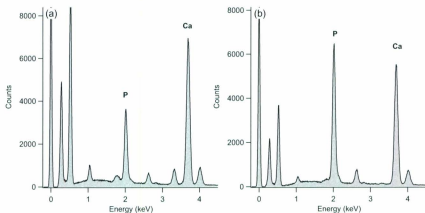


Figure B.2: Energy Dispersive X-ray spectra (EDX) of (a) collagen-hydroxyapatite and (b) collagen-brushite membranes. The EDX spectrum of this collagen-hydroxyapatite membrane has a ratio between the intensities of Ca and P peaks of 1.6, which is consistent with hydroxyapatite ($\text{Ca}_{10}(\text{PO}_4)_6(\text{OH})_2$). The Ca:P intensity ratio for a collagen-brushite membrane is 0.9, which is consistent with brushite ($\text{CaHPO}_4 \cdot 2\text{H}_2\text{O}$).

We use Atomic Force Microscopy (MFP-3D AFM, Asylum Research) and Scanning Electron Microscopy (FEI Quanta 400 environmental SEM) for the analysis of morphology of our collagen-calcium phosphate membranes. The SEM and AFM images show how the various calcium phosphate mineral phases settle over the collagen membranes. In the collagen-hydroxyapatite membrane (prepared with collagen, CaCl_2 and K_2HPO_4), the hydroxyapatite crystals settle well over the entire collagen membrane, and the collagen membrane is not visible. In the collagen-brushite membrane (prepared with collagen, CaCl_2 and $\text{NH}_4\text{H}_2\text{PO}_4$), the brushite settles as a layer over the collagen membrane, and the collagen membrane layers and the fibrils are clearly visible (Figures B.4 and B.3).

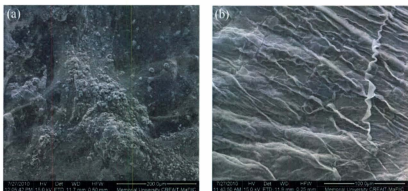


Figure B.3: Scanning Electron Microscope (SEM) images of collagen-hydroxyapatite and collagen-brushite membranes. (a) SEM image of a collagen-hydroxyapatite membrane shows that the hydroxyapatite crystals are well settled over the collagen membrane, and the collagen membrane is not visible because it is in the underneath of hydroxyapatite crystals. (b) SEM image of a collagen-brushite membrane shows that the brushite is settled over the collagen membrane, and the membrane folds are clearly visible.

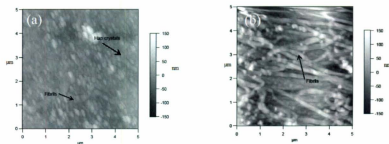


Figure B.4: Atomic Force Microscope (AFM) images of collagen-hydroxyapatite and collagen-brushite membranes. (a) AFM image of a collagen-hydroxyapatite membrane shows crystals over the collagen membrane, and the collagen membrane is not visible because it is underneath. (b) AFM image of a collagen-brushite membrane shows that the brushite is settled over the collagen membrane, and the membrane fibrils are clearly visible.

References

- [1] Kumar, M. R.; Merschrod S., E. F.; Poduska, K. M. *Cryst. Growth Des.* **2011**, *11*, 26-28.
- [2] Kumar, M. R.; Merschrod S., E. F.; Poduska, K. M. *Ceram. Trans* **2010**, *218*, 3-13.
- [3] de Aza, P. N.; Guitián, F.; Santos, C. *Chem. Mater.* **1997**, *9*, 916-922.
- [4] Wisniewski, M.; Sionkowska, A.; Kaczmarek, H.; Lazare, S.; Tokarev, V.; Belin, C. *J. Photochem. Photobio. A: Chem.* **2007**, *188*, 192-199.
- [5] Tsuda, H.; Arends, J. *J. Dent. Res* **1994**, *73*, 1703-1710.
- [6] Jiang, W.; Cheng, J.; Agrawal, D. K.; Malshe, A. P.; Liu, H. *Mater. Res. Soc. Symp. Proc* **2009**, *1140*, 1140-III03-0.
- [7] Bailey, M. S.; Coe, S.; Grant, D. M.; Grime, G. W.; Jeynes, C. *X-Ray Spectrom.* **2009**, *38*, 343-347.
- [8] Juhasz, J. A.; Best, S. M.; Auffret, A. D.; Bonfield, W. *J Mater Sci: Mater Med.* **2008**, *19*, 1823-1829.

